Cell Stem Cell

Article

Recapitulation of endogenous 4R tau expression and formation of insoluble tau in directly reprogrammed human neurons

Graphical abstract

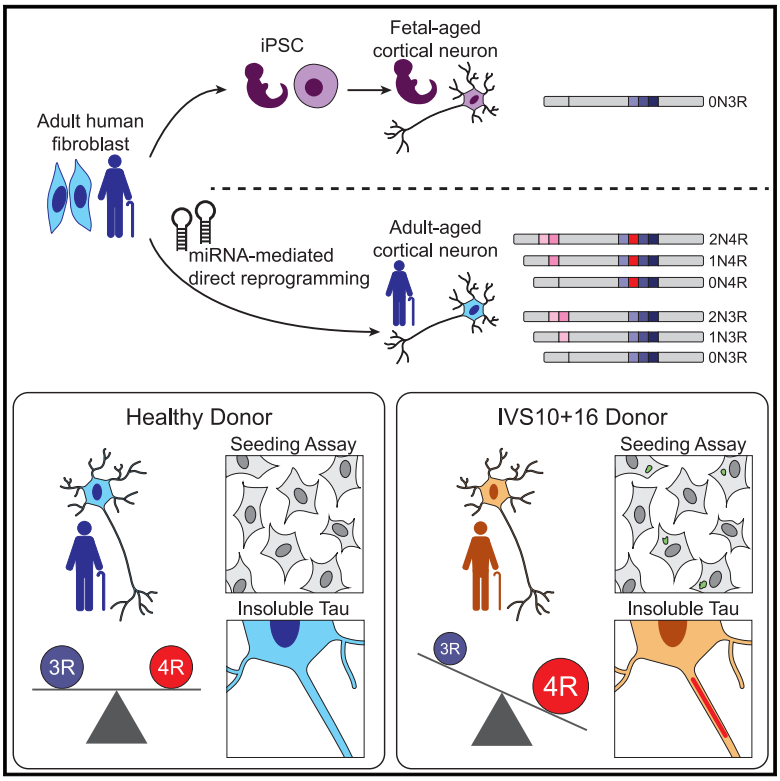

Highlights

- Recapitulation of all adult human tau isoforms in directly reprogrammed neurons
- miNs capture 4R increase caused by familial IVS10+16 splice site mutation
- Patient-derived miNs endogenously generate seed-competent and insoluble tau
- Reduction of tau decreases pathogenic tau species

Authors

Lucia S. Capano, Chihiro Sato, Elena Ficulle, ..., David M. Holtzman, Karen E. Duff, Andrew S. Yoo

Correspondence

k.duff@ucl.ac.uk (K.E.D.), yooa@wustl.edu (A.S.Y.)

In brief

Capano et al. show that human neurons directly reprogrammed by microRNAs from adult fibroblasts capture the endogenous expression of all tau isoforms detected in adult brains, including the vital 1:1 ratio of 3R:4R tau. Also, reprogrammed neurons derived from fibroblasts of tauopathy patients show the formation of seed-capable and insoluble tau.

Capano et al., 2022, Cell Stem Cell *29*, 918–932
June 2, 2022
https://doi.org/10.1016/j.stem.2022.04.018

CellPress

CellPress

Cell Stem Cell

Article

Recapitulation of endogenous 4R tau expression and formation of insoluble tau in directly reprogrammed human neurons

Lucia S. Capano,[1,2,3,12] Chihiro Sato,[4,12] Elena Ficulle,[7,12] Anan Yu,[8,12] Kanta Horie,[4] Ji-Sun Kwon,[1,9] Kyle F. Burbach,[1,10] Nicolas R. Barthélemy,[4] Susan G. Fox,[8] Celeste M. Karch,[5,6,11] Randall J. Bateman,[4,5,6] Henry Houlden,[7] Richard I. Morimoto,[8] David M. Holtzman,[4,5,6] Karen E. Duff,[7,*] and Andrew S. Yoo[1,2,6,13,*]

[1]Department of Developmental Biology, Washington University School of Medicine, St. Louis, MO 63110, USA
[2]Center for Regenerative Medicine, Washington University School of Medicine, St. Louis, MO 63110, USA
[3]Program in Molecular and Cell Biology, Washington University School of Medicine, St. Louis, MO, USA
[4]Department of Neurology, Washington University School of Medicine, St. Louis, MO 63110, USA
[5]Knight Alzheimer's Disease Research Center, Washington University School of Medicine, St. Louis, MO 63110, USA
[6]Hope Center for Neurological Disorders, Knight ADRC, St. Louis, MO 63110, USA
[7]UK Dementia Research Institute at University College London, London WC1E 6BT, UK
[8]Department of Molecular Biosciences, Rice Institute for Biomedical Research, Northwestern University, Evanston, IL 60208, USA
[9]Program in Computational and Systems Biology, Washington University School of Medicine, St. Louis, Missouri, USA
[10]Program in Molecular Genetics and Genomics, Washington University School of Medicine, St. Louis, Missouri, USA
[11]Department of Psychiatry, Washington University School of Medicine, St. Louis, MO 63110, USA
[12]These authors contributed equally
[13]Lead contact
*Correspondence: k.duff@ucl.ac.uk (K.E.D.), yooa@wustl.edu (A.S.Y.)
https://doi.org/10.1016/j.stem.2022.04.018

SUMMARY

Tau is a microtubule-binding protein expressed in neurons, and the equal ratios between 4-repeat (4R) and 3-repeat (3R) isoforms are maintained in normal adult brain function. Dysregulation of 3R:4R ratio causes tauopathy, and human neurons that recapitulate tau isoforms in health and disease will provide a platform for elucidating pathogenic processes involving tau pathology. We carried out extensive characterizations of tau isoforms expressed in human neurons derived by microRNA-induced neuronal reprogramming of adult fibroblasts. Transcript and protein analyses showed that miR neurons expressed all six isoforms with the 3R:4R isoform ratio equivalent to that detected in human adult brains. Also, miR neurons derived from familial tauopathy patients with a 3R:4R ratio altering mutation showed increased 4R tau and the formation of insoluble tau with seeding activity. Our results collectively demonstrate the utility of miRNA-induced neuronal reprogramming to recapitulate endogenous tau regulation comparable with the adult brain in health and disease.

INTRODUCTION

Tauopathies are adult-onset, neurodegenerative disorders whose shared pathology is intracellular tau protein aggregates (Gao et al., 2018; Götz et al., 2019). Tau, encoded by the microtubule associated protein tau (*MAPT*) gene, produces six protein isoforms whose expression is under strict developmental regulation, with only one isoform (0N3R) present during fetal development but all six present perinatally and maintained throughout the life span (Goedert and Jakes, 1990; Goedert et al., 1989b; Hefti et al., 2018; Himmler et al., 1989). Tau isoforms are defined by the inclusion or exclusion of three alternatively spliced exons: 2, 3, and 10. Exons 2 and 3 inclusion produces two N-terminal domains (N1 and N2), whereas exon 10 encodes the second imperfect-repeat microtubule-binding domain (R2) among three other repeat domains (R1, R3, and R4) (Goedert et al., 1989a). The inclusion or exclusion of exon 10 gives rise to 4-repeat (4R) and 3-repeat (3R) tau, respectively, and these two isoform families are expressed at an approximately 1:1 ratio in the healthy adult human brain (Goedert et al., 1989a; Kosik et al., 1989). Perturbation of the 3R:4R tau ratio contributes to the pathogenesis of various tauopathies, and of the 53 known familial pathogenic tau mutations, almost 50% are located within or related to the expression of exon 10 (Ghetti et al., 2015). Thus, it is critical to establish a human neuron-based system that recapitulates the endogenous tau isoforms seen in the adult brain and tau pathology resulting from 3R:4R dysregulation in patient-derived neurons. The significance of human neuron-based approaches is also highlighted by the fact that humanized mouse tau models lack the 1:1 3R:4R ratio and requires genetic

perturbation to achieve 3R:4R tau level comparable with the adult human brain (Duff et al., 2000; He et al., 2020).

The past decade has primarily used neuronal differentiation of induced pluripotent stem cells (iPSCs) as the primary methodology for generating human neurons (iPSC-Ns). Although these cells offer a robust means to generate neurons at a large quantity, their utility in studying processes that occur in aged neurons has been limited due to the reversion of the cellular age, and previous studies revealed that iPSC-Ns represent fetal stages of development (Lapasset et al., 2011; Patterson et al., 2012) and express only marginal levels of 1N, 2N, and 4R tau expressions (Ehrlich et al., 2015; Sato et al., 2018; Sposito et al., 2015). To increase 4R tau levels in iPSC-Ns, several experimental perturbations have been used, including transgene overexpression (Verheyen et al., 2015), splicing mutations (Verheyen et al., 2018), or extended culturing times (188–365 days) (Beevers et al., 2017; Sposito et al., 2015). However, these experimental manipulations still fall short of generating neurons with the endogenous ratio of 3R:4R in the adult human brain. Only the immortalized human neural progenitor ReNcells, after differentiation into a neuronal population, have expressed 4R tau mRNA along with 3R tau (Choi et al., 2014; Kwak et al., 2020). ReNcells serve as a model for human neurons but will have to be engineered to carry known human tau mutations. Therefore, an alternative strategy to generate human neurons that mirror the endogenous tau expression and harbor familial mutations will greatly increase the ability to study tauopathies.

Brain-enriched microRNAs (miRNAs) miR-9/9* and miR-124 (miR-9/9*-124) are potent neurogenic miRNAs whose expression is present in fetal and adult brain. During neural development, these miRNAs regulate cell proliferation and neuronal differentiation (Lim et al., 2005; Tan et al., 2012; Zhao et al., 2009). When ectopically expressed in human adult fibroblasts, miR-9/9*-124 can directly convert fibroblasts to neurons (miNs) (Lu and Yoo, 2018; Yoo et al., 2011). The miRNA-induced neuronal state can be synergized with subtype-defining transcription factors (TFs) that guide conversion to specific neuronal subtypes (Abernathy et al., 2017; Victor et al., 2014). During reprogramming, miRNAs first instruct cell cycle exit and fibroblast identity erasure, followed by the neuronal program activation in sequence (Cates et al., 2021). The fate conversion relies on miRNAs targeting components of chromatin modifiers and TFs, coordinating extensive reconfiguration of chromatin landscape without passing through pluripotent and multipotent stem cell stages (Abernathy et al., 2017; Cates et al., 2021; Huh et al., 2016; Richner et al., 2015; Victor et al., 2018; Yoo et al., 2009). This property in turn allows for the maintenance of the epigenetic age signature of fibroblast donors (Huh et al., 2016). Additionally, modeling adult-onset disorders using miNs derived from symptomatic Huntington's disease patients exhibited hallmark adult-onset pathologies such as Huntingtin inclusion bodies, whereas their iPSC-N counterparts failed to do so (Victor et al., 2018).

Here, we reveal that miRNA-mediated direct reprogramming generates human neurons that express both 3R and 4R tau in the same ratio detected in adult human brains. RNA profiling by transcript assays and protein profiling by mass spectrometry demonstrates that adult human brain and miNs from adult fibroblasts have indistinguishable 4R tau profiles, which starkly contrasts with the low 4R tau expression in primary fetal human neurons and iPSC-Ns. The endogenous tau isoform regulation in miNs is sensitive to a point mutation within the splice site proximal to exon 10 in tauopathy patients resulting in reprogrammed neurons that showed increased 4R:3R tau ratio. Significantly, the increased level of 4R tau correlated with the formation of insoluble tau and seed-competent tau, reminiscent of that seen in human 4R tauopathies, and contrasting the lack of seed-competent tau seen in iPSC-Ns harboring the same patient mutation. Therefore, miRNA-mediated neuronal reprogramming provides a robust model for studying both the normal and abnormal biology of tau and exon 10 pathological mutations.

RESULTS

MiNs display neuronal markers similar to iPSC-Ns and fibroblast fate erasure

In this study, we adapted the neuronal conversion protocol based on miR-9/9*-124, neuronal differentiation 2 (NEUROD2), and myelin transcription factor 1-like (MYT1L) TFs to generate neurons of cortical lineage (Yoo et al., 2011) (Figure 1). To minimize the number of lentiviruses used for transduction in fibroblasts, we replaced *NEUROD2* with ISX9, a neurogenic compound that has been previously shown to activate endogenous NEUROD-family TFs (Li et al., 2015).

At 30 days post-induction (PID 30), immunostaining for pan-neuronal marker neuronal cell adhesion molecule 1 (NCAM1) showed a robust reprogramming output with miNs displaying extensive process outgrowths (Figure 1A left, bottom-left: zoomed in view of NCAM1 expression). The reprogrammed cells were also enriched for other pan-neuronal markers, microtubule associated protein 2 (MAP2) (Figure 1A, bottom-right), and neurofilament heavy chain (Figure 1A, right). Beta III tubulin (TUBB3) was used to monitor cell morphologies. Importantly, immunostaining against tau revealed the miN population highly enriched with tau expression showing prototypical patterns of tau islands in TUBB3-positive outer neurites (Figure 1B), an endogenous tau feature suggested to be reflective of tau-tau interactions (Siahaan et al., 2019; Tan et al., 2019).

Using immunocytochemistry on four independent fibroblast samples reprogrammed into miNs (Figure 1C), approximately 60%–70% of DAPI-positive cells showed MAP2- and tau-positivity, which is consistent with the reprogramming efficiency previously reported (Abernathy and Yoo, 2015; Cates et al., 2021; Huh et al., 2016; Victor et al., 2014; Victor et al., 2018). qPCR analyses of neuronal genes, *MAP2*, *NEFL* (neurofilament light chain), *MAPT*, and the glutamatergic marker, *SLC17A7* (also known as *VGLUT1*), showed enrichment over starting fibroblasts (Figure 1D). Also, qPCR analyses of the cortical markers *TBR1* (T-box brain TF 1), *MEF2C* (myocyte enhancer factor 2C), *BRN2* (POU class 3 homeobox 2), and *NEUROD2* demonstrated that the combination of MYT1L and ISX9 are sufficient to drive the cortical fate (Figure 1E).

Using single-cell RNA-sequencing (scRNA-seq) to stratify starting fibroblasts (n = 2,533), reprogrammed miNs (n = 9,305), and iPSC-Ns (n = 7,212) by their transcriptome, we identified three distinct cell populations corresponding to fibroblasts, miNs, and iPSC-Ns (Figure 1F, left). For instance, the non-neuronal marker *SERPINE1* (Docagne et al., 1999; Mehra

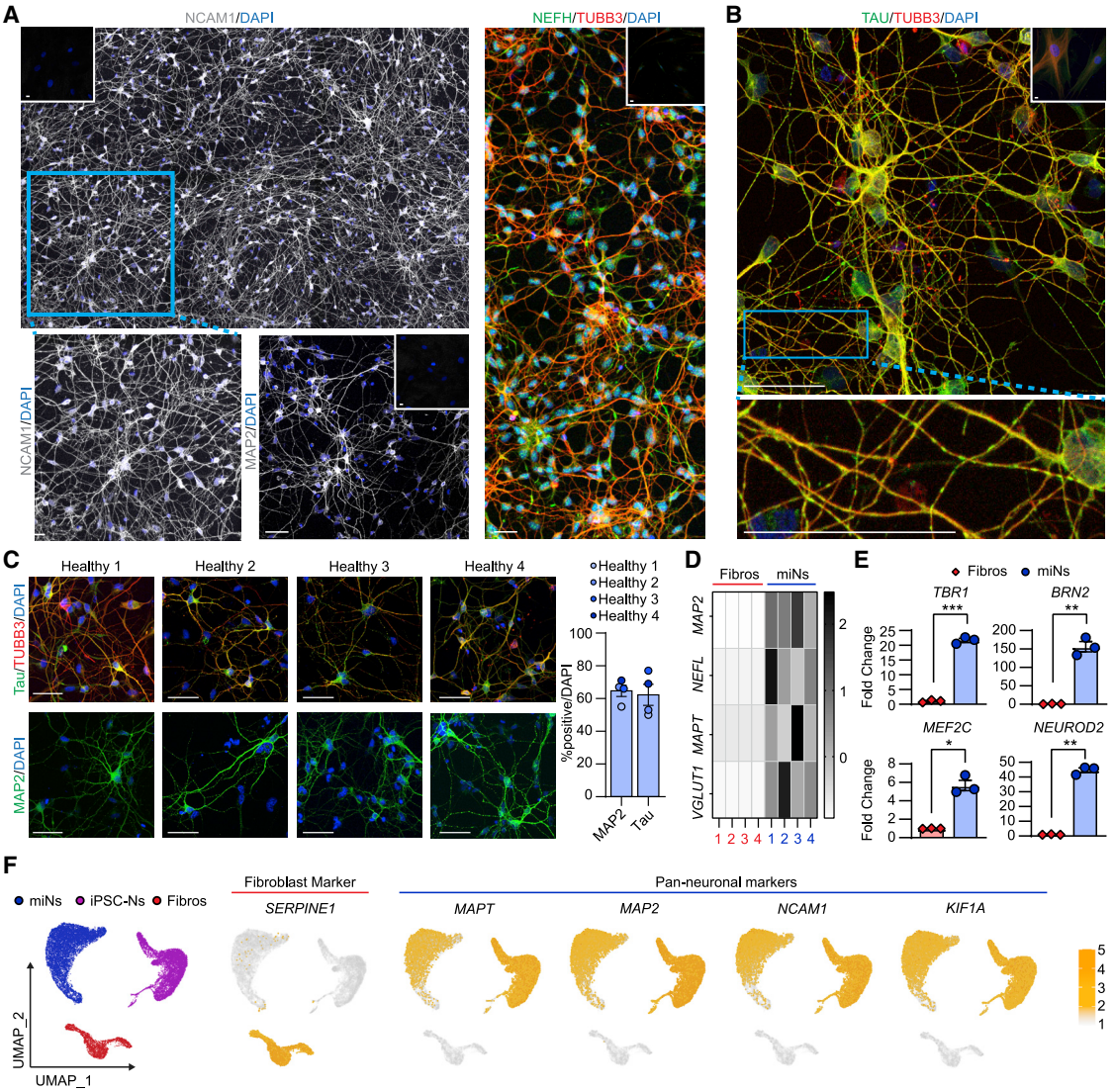

Figure 1. Directly reprogrammed neurons display neuronal morphology and transcriptome

(A) Representative images of miNs from healthy adult individuals (healthy 3 + 4) at post-induction day (PID) 30 immunostained with NCAM (composite of 3 × 2 40× images stitched together), MAP2, NEFH, and TUBB3. Insets at the corners are immunostaining images performed in starting fibroblasts. Blue rectangular outline depicts the region shown in magnified images. Scale bars, 50 μm.

(B) Representative image of healthy 4 immunostained for total tau and TUBB3. Inset is starting fibroblasts. Blue rectangular outline depicts the magnified region showing tau islands. Scale bars, 50 μm.

(C) Left, representative images of healthy miNs stained for tau and TUBB3. Right, quantification of % positive over DAPI in reprogrammed cells from four independent fibroblast samples (MAP2, number of cells counted: miN 1 = 140, miN 2 = 82, miN 3 = 112, and miN 4 = 169; MAPT Ns: miN 1 = 113, miN 2 = 118, miN 3 = 78, and miN 4 = 87). Scale bars, 50 μm. Mean ± SEM.

(D) Heatmap plots Z-scores comparing qPCR of neuronal genes between miNs and starting fibroblasts from four independent samples.

(E) Fold change of cortical genes between starting fibroblasts and day 30 miNs. n = 3 replicates from miNs grown in three independent wells. Mean ± SEM; two-tailed Student's t test; *p ≤ 0.05, **p ≤ 0.01, ***p ≤ 0.001.

(F) Left, UMAP projection of cells colored by starting cell type (fibroblast: n = 2,533 cells; iPSC-N: n = 7,212 cells; miN: n = 9,305 cells). Right, UMAP projection of cells colored by non-neuronal (*SERPINE1*) and pan-neuronal markers (*MAPT*, *MAP2*, *NCAM1*, and *KIF1A*).

See also Figure S1.

et al., 2016) was enriched only in starting fibroblasts, whereas the miNs and iPSC-Ns demonstrated thorough expression of pan-neuronal markers, *MAPT*, *MAP2*, *NCAM1*, and *KIF1A* (Figure 1F, right). Additionally, miNs were characterized by the high expression of *SLC17A7* (*VGLUT1*), whereas iPSC-Ns were positive for *SLC17A6* (*VGLUT2*) (Figures S1A–S1C). MiNs and iPSC-Ns expressed different glutamate receptor subunits, but both were highly enriched for the glutamine synthetase, *GLUL*. *GAD1* and *GAD2* were present in a subset of miNs and iPSC-Ns, respectively. However, the expression of GABA transporter *SLC6A1*, representing inhibitory cell fate, was only marginal. MiNs showed a low number of *PVALB*-positive cells,

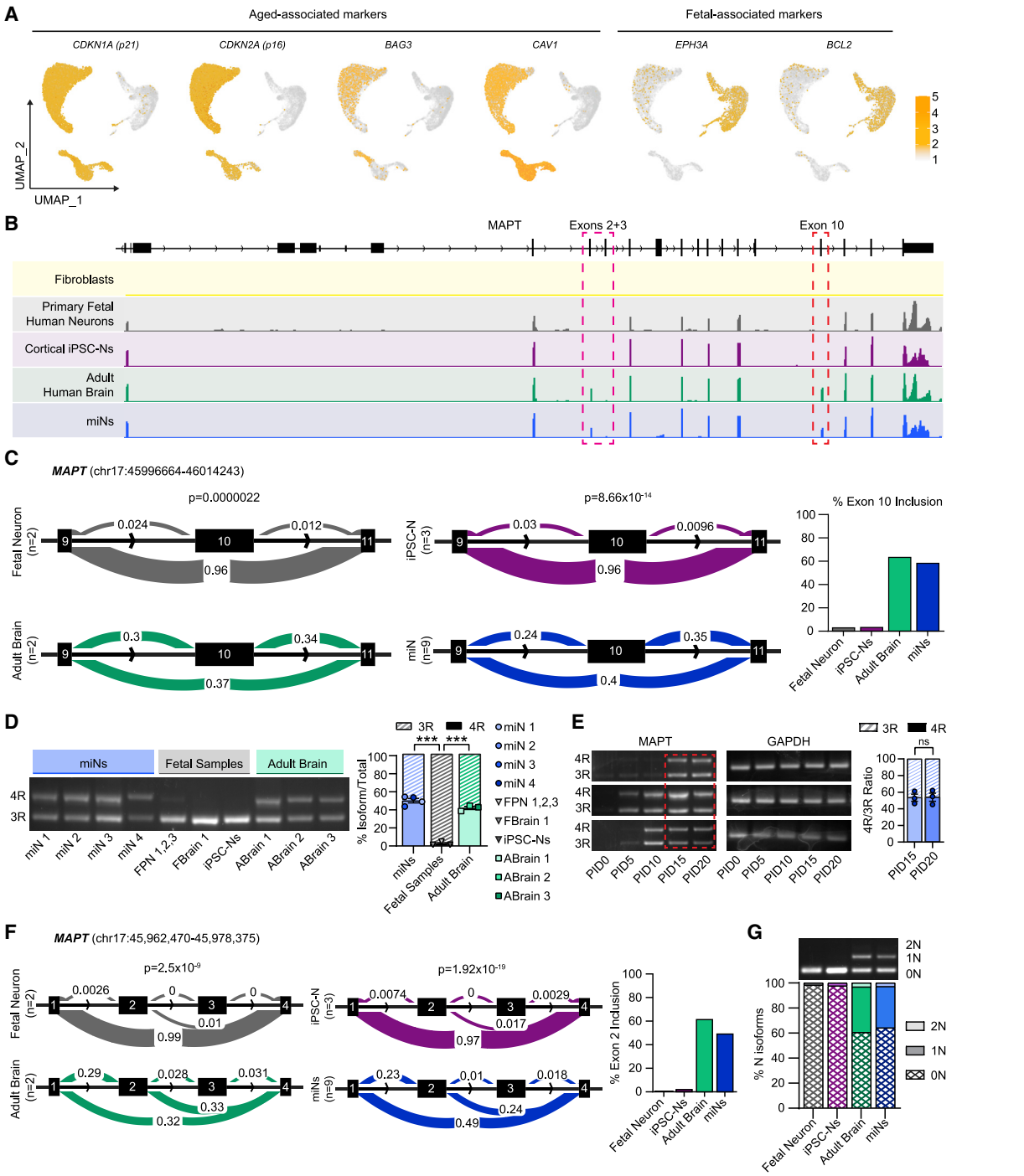

Figure 2. MiNs express exon 10 inclusion at equivalent ratio to the adult human brain

(A) UMAP projection of cells colored by age-associated markers (*CDKN1A*, *CDKN2A*, *BAG3*, and *CAV1*) and fetal-associated markers (*EPHA3* and *BCL2*). Cell numbers as indicated in Figure 1F.

(B) Representative RNA-seq tracks at the MAPT locus of fibroblasts, primary human neurons, cortical iPSC-Ns, adult human brain, and miNs at PID21.

(C) Leafcutter analysis of *MAPT* exon 10 inclusion between fetal neurons and adult brain, and healthy iPSC-Ns and healthy miNs. Percent exon 10 inclusion is quantified on the right. For primary fetal neurons and adult brain, n= sequencing replicates were performed from purchased purified RNA (see STAR Methods). For iPSC-Ns, n = replicates grown in three independent wells. For miNs, n = three independent well replicates from three independent individuals.

(D) Left, semi-quantitative PCR of 3R and 4R tau isoforms. Right, Quantification of 3R and 4R percent ratio of samples grouped by miNs, fetal samples, and adult brain from independent individuals as indicated in the graph legend. Mean ± SEM; one-way ANOVA with multiple comparisons with post hoc Tukey's test; ***p $\leq$ 0.001.

(legend continued on next page)

whereas iPSC-Ns had small populations of *SST* and *TH* positive cells. Together, these results support the notion that miNs robustly acquire a neuronal fate due to miRNA-mediated reprogramming.

Age-maintained miNs endogenously express a 1:1 3R:4R tau isoform ratio equivalent to adult brain

ScRNA-seq revealed that age-associated markers as main drivers for distinct segregation of miNs and iPSC-Ns. For instance, miNs were positive for the advanced-age markers *CDKN1A* (p21), *CDKN2A* (p16), *BAG3*, and *CAV1* (Figure 2A). *BAG3* expression dramatically increases with aging in mouse neurons (Gamerdinger et al., 2009) and the human brain (brainspan.org) and has been implicated in tau clearance (Lei et al., 2015). The expression of *CAV1* has been shown to be increased in aged human brains (Kang et al., 2006), and its abnormal expression has been implicated in Parkinson's disease (Ha et al., 2021). In contrast, fetal-associated markers such as *EPH3A* (brainspan.org) and *BCL2* (Merry et al., 1994) were enriched in iPSC-Ns. These results conform to previous studies indicating the maintenance of cellular age in direct neuronal reprogramming (Huh et al., 2016; Mertens et al., 2015).

Tau isoform expression is developmentally regulated in which 4R isoforms begin to be expressed perinatally and are maintained throughout adulthood (Hefti et al., 2018). Extending the notion of age maintenance, we tested if miNs expressed 4R tau by bulk RNA-sequencing (RNA-seq). Strikingly, miNs and adult brain showed robust signal of exon 10 in the RNA-seq tracks (Figure 2B, red dashed box: blue and green tracks, respectively), peaks that were distinctly missing in primary fetal human neurons and iPSC-Ns (Figure 2B, red dashed box: gray and purple tracks, respectively). The alternatively spliced exons 2 and 3 are also clearly expressed in miNs and the adult human brain (Figure 2B, pink-dashed box). Using Leafcutter to calculate splicing events (Li et al., 2018), we quantified inclusion of exon 10 and found significant differences between fetal (3.6%) and adult brain (64%) ($p = 2.2 \times 10^{-6}$) and iPSC-Ns (3.9%) and miNs (59%) ($p = 8.66 \times 10^{-14}$) (Figure 2C). Leafcutter also identified 630 genes that demonstrate similar and significant differences in alternative splicing between adult brain versus fetal neurons, also manifested in miNs versus iPSC-Ns (Table S1). Some known age-associated splicing events captured between our aged and fetal samples include *SCN2A* (Kasai et al., 2001; Thompson et al., 2020), *DCTN4* (Tanner et al., 2021), *MAPRE3* (Mazin et al., 2013), and *NEO1* (Mazin et al., 2013) (Figure S2A).

To specifically look at the 3R to 4R tau mRNA ratio, we used semi-quantitative PCR (sq-PCR) (Marone et al., 2001) in which PCR is performed in a cDNA library with primers in exons 9 and 12, flanking exon 10, creating a long (4R) and short (3R) PCR product corresponding to the inclusion and exclusion of exon 10, respectively. Using ImageJ (Abramoff et al., 2004) to quantify, we found consistent expression of 4R tau mRNA in miNs comparable with adult human brain samples, whereas all three types of fetal samples primarily expressed 3R tau (Figure 2D). MiNs were found to express 50.3% of tau mRNA as 4R tau (Figure 2D, right). We asked at what time point during the neuronal reprogramming tau expression begins, and in multiple fibroblast samples we found consistent, robust expression of both 3R and 4R tau transcripts starting at PID15 (Figure 2E). Of note, this two-week point corresponds to the time that miNs start activating the neuronal program required for neuronal identity (Cates et al., 2021).

In addition to exon 10, *MAPT* exons 2 and 3 are also spliced under developmental control, with fetal samples only expressing a singular 0N isoform, whereas the adult human brain expresses around 40% 0N, 50% 1N, and 10% 2N isoforms (Goedert and Jakes, 1990). Leafcutter determined that the inclusion of exon 2 was also differentially spliced between adult versus fetal samples, also reflected in miNs versus iPSC-Ns, where the fetal-aged samples showed no inclusion, but adult-aged samples expressed ~50% 1N isoforms (Figure 2F). To validate, we designed sqPCR primers that flank exons 2 and 3, generating long, medium, and short PCR products corresponding to 2N, 1N, and 0N isoform transcripts, respectively. Fetal-aged samples only expressed 0N isoforms, whereas adult brain and miNs had equivalent expression of all three N isoforms (Figure 2G).

To determine if the miRNAs were controlling the inclusion of exon 10, we overexpressed either nonspecific miRNAs or miR-9/9*-124 in neural progenitor cells (NPCs) and then differentiated them to iPSC-Ns through small molecule differentiation (Mahali and Karch, 2021). Neither nonspecfic nor miR-9/9*-124 affected exon 10 inclusion, and all iPSC-N samples expressed only 3R tau (Figure S2B). These data support that miNs maintain the age of the starting cells (Huh et al., 2016), and this age drives exon 10 inclusion, leading miNs to recapitulate the endogenous 4R expression, generating the 1:1 3R:4R ratio seen in the adult brain.

What controls exon 10 inclusion has not been identified in the adult human brain context. It is possible that age-associated, differentially expressed RNA binding proteins and splicing factors direct the inclusion of exon 10 in adult-aged samples. We compared pairwise, bulk RNA-seq between adult brain versus fetal neurons and miNs versus iPSC-Ns and identified 88 differentially expressed genes identified by ingenuity pathway analysis as splicing regulators (Table S2). This gene list will have to be validated for potential age-associated splicing regulators in future studies.

MiNs produce endogenous 4R tau protein similar to adult brain

To validate tau isoform expression at the protein level, we performed mass spectrometry that can quantitatively and sensitively

(E) Semi-quantitative PCR of 3R and 4R tau expressions. Red rectangular outline depicts the time point when 4R tau starts being expressed consistently in multiple samples (n = three independent individuals). Right, two-tailed Student's t test of PID15 versus PID20. Mean ± SEM; ns p = 0.92.

(F) Leafcutter analysis of *MAPT* exons 2 and 3 between fetal neurons and adult brain and iPSC-Ns and miNs as in (C). Percent exon 2 inclusion is quantified on the right.

(G) Top, semi-quantitative PCR of 0N, 1N, and 2N *MAPT* isoforms. Bottom, quantification of N isoform percentages of fetal neuron, iPSC-N, adult brain, and miN samples.

See also Figure S2 and Tables S1 and S2.

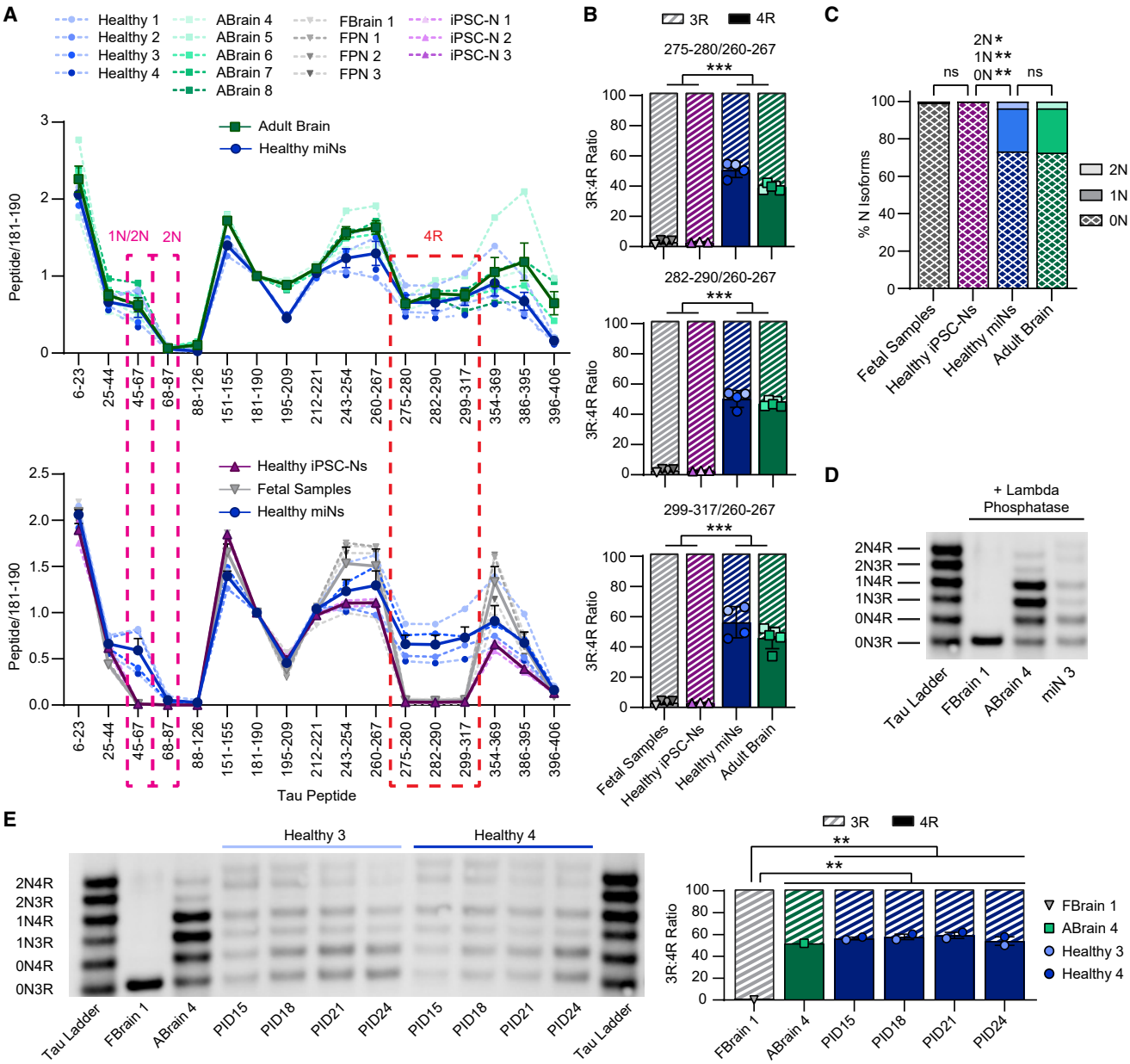

Figure 3. MiN tau protein profile mirrors that of the adult human brain

(A) Quantitation of relative tau peptides from multiple independent samples as indicated in the plot legend. Mean (thick line) ± SEM. Pink and red dashed outline depicts 1N/2N-, 2N-, and 4R-specific tau peptides, respectively.

(B) Quantification of 3R:4R isoform ratio of all samples used in (A). Histogram colors are matched to sample colors shown in the plot legend of (A). Mean ± SEM; one-way ANOVA with multiple comparisons and post hoc Tukey's test: between any fetal versus adult sample for all three 4R peptides: ***$p \leq 0.001$.

(C) Percent of N isoforms (calculation in methods) using all samples as indicated in the plot legend in (A). Mean ± SEM; one-way ANOVA with multiple comparisons and post hoc Tukey's test. All N isoforms between fetal versus healthy iPSC-Ns and between adult versus healthy miNs: ns $p > 0.999$; between healthy iPSC-Ns versus healthy miNs: 0N: **$p = 0.002$, 1N: **$p = 0.002$, 2N: *$p = 0.015$.

(D) Western blot of tau isoforms.

(E) Left, western blot of tau isoforms over reprogramming time course. Right, quantification of 3R:4R ratio from 0N and 1N isoforms during the time course of reprogramming of two independent samples as indicated in the plot legend. Mean ± SEM; one-way ANOVA with multiple comparisons and post hoc Tukey's test; between fetal versus any miN: **$p = 0.002$; between fetal and adult-aged samples: **$p = 0.004$.

measure the tau isoforms in both cell culture and brain (Barthélemy et al., 2020a, 2020b; Horie et al., 2020; Sato et al., 2018) on miNs from four independent adult individuals, four independent samples of fetal primary neurons or brain, adult brains from five individuals, and three iPSC-N replicates (Figure 3A, solid line = mean). We quantified tau peptides across full-length intracellular

tau protein, including peptides specific for 4R (residues 275–280, 282–290, and 299–317). In iPSC-Ns and fetal samples, the 1N, 2N, and 4R peptides were expressed at less than 3% of the sum of all tau isoforms (i.e., 0N+1N+2N and 3R+4R, respectively) (Figures 3A–3D), consistent with previous literature showing iPSC-Ns recapitulate only fetal neuronal tau isoforms (Ehrlich et al., 2015; Sato et al., 2018; Sposito et al., 2015). Importantly, the 1N, 2N, and 4R peptide profiles of miNs showed significant enrichment over that of fetal samples, mirroring the tau profile of the adult brain samples (Figures 3A–3D). To specifically assay 3R:4R in miNs, we analyzed the ratio of all three 4R-specific peptides to the adjacent, constitutive R1 domain peptide (260–267). Remarkably, miNs display an approximately 1:1 3R to 4R ratio equivalent to that of the adult human brain, which drastically contrasted iPSC-Ns and fetal neurons (Figures 3A and 3B). The presence of multiple tau isoforms in miNs and adult brain was confirmed via western blot, which differed with fetal brain expressing only 0N3R isoform (Figure 3D). Furthermore, a time course of a western blot for tau in miNs at days 15–24 into reprogramming showed clear expressions of both 3R and 4R isoforms at 1:1 3R:4R ratio throughout the immunoblots (Figure 3E).

Directly reprogrammed miNs from tauopathy patient fibroblasts recapitulate abnormal 4R tau mRNA expression

We next asked if the neuronal reprogramming would be sensitive to capture the increased 4R tau resulting from a point mutation at an intronic splice site known as IVS10+16 C>T (IVS10+16) (Hutton et al., 1998), which disrupts a stem-loop structure and biases splicing toward exon 10 inclusion (Grover et al., 1999). This familial mutation was shown to cause an approximately 2-fold to 4-fold increase in 4R tau mRNA (Connell et al., 2005) and an imbalanced 3R:4R protein ratio, skewing toward increased 4R. First, we directly converted fibroblast samples with confirmed mutation status (Figures S3A and S3B) from four symptomatic patients, quantifying successful neuronal conversion, with 75% of DAPI-positive cells expressing MAP2 and tau (Figure 4A). IVS10+16 miNs showed enrichment of neuronal genes over their starting fibroblasts (Figure 4B). Neurons are different from most other cell types in their robust expression of long genes (>100 kb) (Gabel et al., 2015; King et al., 2013; Sugino et al., 2014). Using LONGO, a gene length analysis R package (McCoy et al., 2018), we found miNs from both healthy control and IVS10+16 fibroblasts were successfully reprogrammed to neurons as seen by the forked trajectory between miNs and fibroblasts starting around 200 kb (Figure 4C). Reprogrammed miNs had significantly higher long gene expression over the starting fibroblasts ($p < 0.001$), but there was no significant difference in long gene expression between healthy and IVS10+16 miNs ($p=0.177$), indicating a similar conversion efficiency and no effect of the IVS10+16 mutation on neuronal reprogramming.

We next used Leafcutter on bulk RNA-seq to dissect the amount of exon 10 inclusion between healthy and IVS10+16 miNs and found that there was a significant increase in 4R tau in IVS10+16 samples ($p = 0.012$) (Figure 4D). This was validated using sq-PCR in which IVS10+16 miNs had a significant increase in exon 10 inclusion over that of healthy miNs and adult brain, with a 1.46-fold increase in their 4R:3R mRNA ratio (Figure 4E). As this fold change differed from those published when this familial mutation was discovered (Hutton et al., 1998), we performed sqPCR on IVS10+16 human brain and found the same fold change between IVS10+16 miNs and human brain over their corresponding healthy controls (Figure 4F). As expected, N isoform expression ratios were not altered in IVS10+16 miNs (Figure S3C).

Increase in 4R tau protein in IVS10+16 miNs

To validate the increase in 4R mRNA on the protein level, we performed mass spectrometry analyses on four independent patient-derived IVS10+16 miNs and IVS10+16 iPSC-Ns, both of which demonstrated an increase in the 4R tau peptides over the age-matched, healthy counterparts (Figure 5A, solid line = mean). IVS10+16 miNs had a significant increase in all three 4R-specific peptides over that of healthy miNs (Figure 5B). IVS10+16 iPSC-Ns also showed a significant increase in 4R tau over isogenic healthy iPSC-Ns, but their final 4R tau expression remains far below that of the 3R tau level (Figure 5A bottom: purple line, Figure 5B: pink bars). The ratio of all three 4R-specific peptides matched the increase seen in mRNA, with a 1.31-fold to 1.41-fold increase in the IVS10+16 patient miNs over the healthy miNs (Figure 5C). As expected, there was no significant difference in the profile of any other regions of tau including the ratio of 0N, 1N, or 2N isoforms between WT and IVS10+16 miNs (Figure 5D).

Increased insoluble tau and seeding capacity in IVS10+16 miNs

As a model system that endogenously expresses both the altered 3R:4R tau ratio seen in patient samples and has the advanced-age required for tau-associated phenotypes, we assessed IVS10+16 miNs for human tauopathy-specific pathologies. Previous studies have indicated that pathological tau has seeding capacity that precedes the formation of insoluble tau (Holmes et al., 2014) and which can be assayed using a tau-based Fluorescence Resonance Energy Transfer (FRET) Biosensor Assay (Clavaguera et al., 2009; Frost et al., 2009; Guo and Lee, 2011; Liu et al., 2012). We found the patient-derived IVS10+16 miNs produced seeding-competent tau, with a 50% increase in FRET-positive signal from IVS10+16 miN lysate over that of healthy miN lysate (Figure 6A), indicating the presence of tau seeds. Importantly, healthy and isogenic IVS10+16 iPSC-Ns did not show any seeding capacity (Figure 6A).

We next used methanol fixation method to remove soluble proteins (Guo et al., 2016; Katsikoudi et al., 2020) and stained with five tau-specific antibodies: AT8, (phospho-Ser202/Thr205), CP13 (pS202 tau), PHF1 (phosphor-Ser396/Ser404), TOC1 (oligomeric tau), and MC1 (conformationally abnormal tau). All five antibodies showed a significant increase in signal in IVS10+16 miNs over that of healthy miNs, indicating the increased presence of insoluble tau in patient-derived miNs (Figure 6B). No exogenous perturbation was applied to these cells; the insoluble tau developed through endogenous methods. This is in striking contrast to previously published data from IVS10+16 iPSC-Ns, which were devoid of insoluble tau (Verheyen et al., 2018). We also observed thread-like tau staining (Braak and Del Tredici, 2010; Guo et al., 2016; Katsikoudi et al., 2020) in IVS10+16 miNs (Figure 6C). By using a stimulated emission depletion (STED) confocal microscope, we obtained higher resolution images of CP27-positive insoluble tau that

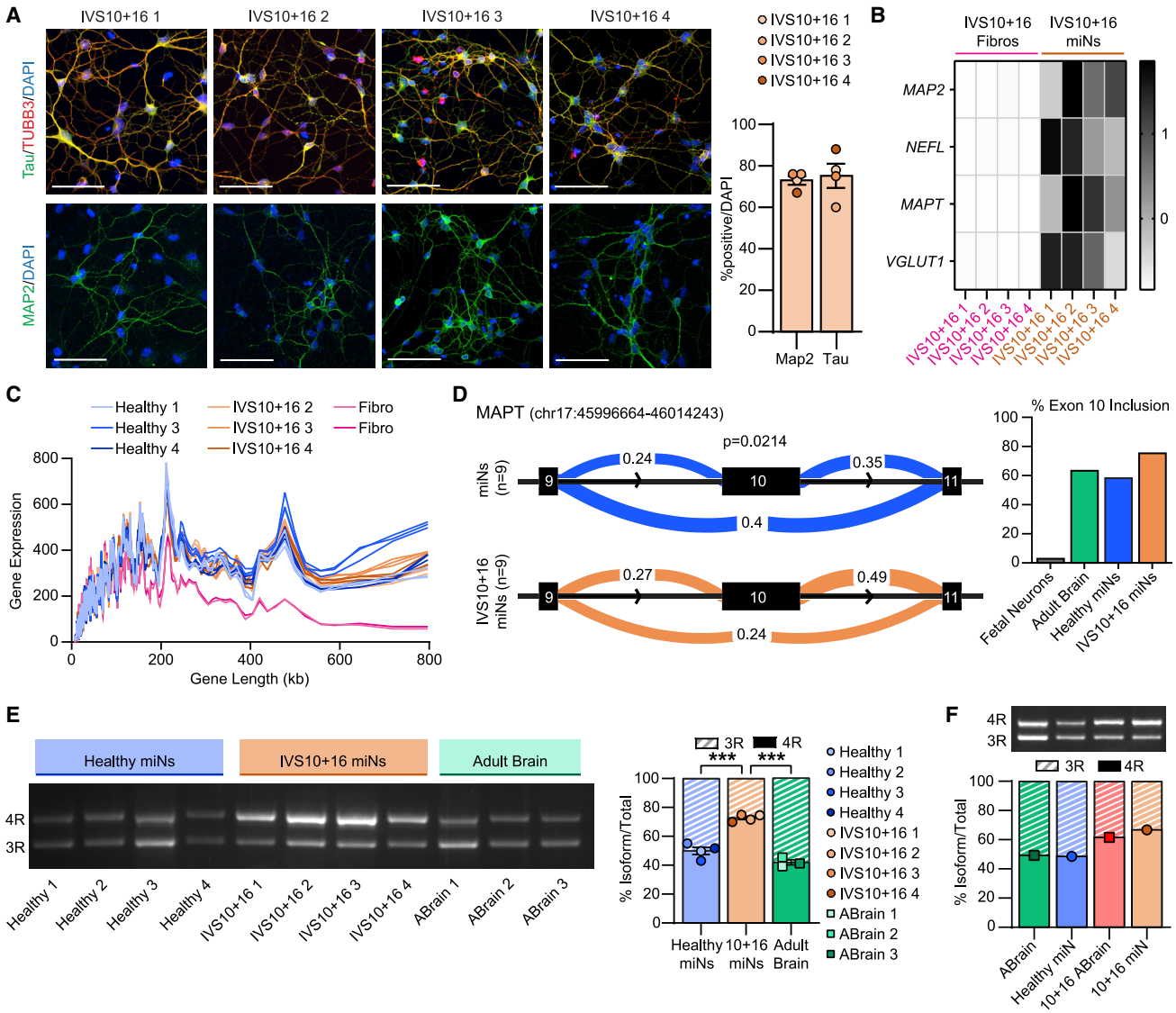

Figure 4. IVS10+16 patient-derived miNs show increased 4R tau mRNA

(A) Left, representative images of reprogrammed IVS10+16 miNs from four independent, symptomatic IVS10+16 patients, immunostained for tau, MAP2, and TUBB3. Right, quantification of % positive over DAPI (MAP2 number of cells counted: IVS10+16 1 = 118, IVS10+16 2 = 173, IVS10+16 3 = 105, and IVS10+16 4 = 152; MAPT number of cells counted: IVS10+16 miN 1 = 98, IVS10+16 miN 2 = 125, IVS10+16 miN 3 = 89, and IVS10+16 miN 4 = 88). Scale bars, 50 μm.

(B) *Z* score heatmap (from qPCR) representation of neuronal marker gene expression *MAP2*, *NEFL*, *MAPT*, and *VGLUT1* in IVS10+16 miNs and starting fibroblasts from four independent lines.

(C) LONGO long gene analysis between starting fibroblasts (red) and reprogrammed healthy miNs (blue) and IVS10+16 miNs (orange).

(D) Leafcutter analysis of *MAPT* exon 10 inclusion between healthy and IVS10+16 miNs. Percent exon 10 inclusion is quantified on the right. For miN groups, n = three independent well replicates from three independent individuals.

(E) Left, sqPCR for detecting 4R and 3R tau ratios. Right, sqPCR intensity values grouped by healthy miNs, IVS10+16 miNs, and healthy adult brain for 3R and 4R. Mean ± SEM. One-way ANOVA with multiple comparisons and post hoc Tukey's test; Between both healthy miNs versus IVS10+16 miNs and IVS10+16 miNs versus adult brain: ***$p \leq 0.001$.

(F) sqPCR for 3R:4R isoform ratio of both healthy and IVS10+16 human brain and miNs.

See also Figure S3.

demonstrated speckles of varying sizes along the neurites imaged (Figure 6D). We further confirmed that the insoluble tau signal was specific and caused by the tau protein by applying tau siRNA to IVS10+16 miNs. The total tau was reduced by 30%–40% (Figure S4), which led to a significant reduction in the amount of insoluble tau (Figure 6E).

DISCUSSION

The ability to study tau expression, isoform control, and age-associated disease pathologies will rely on a model system that endogenously recapitulates tau expression of the adult human brain. ReNcell-derived neurons display a dramatic

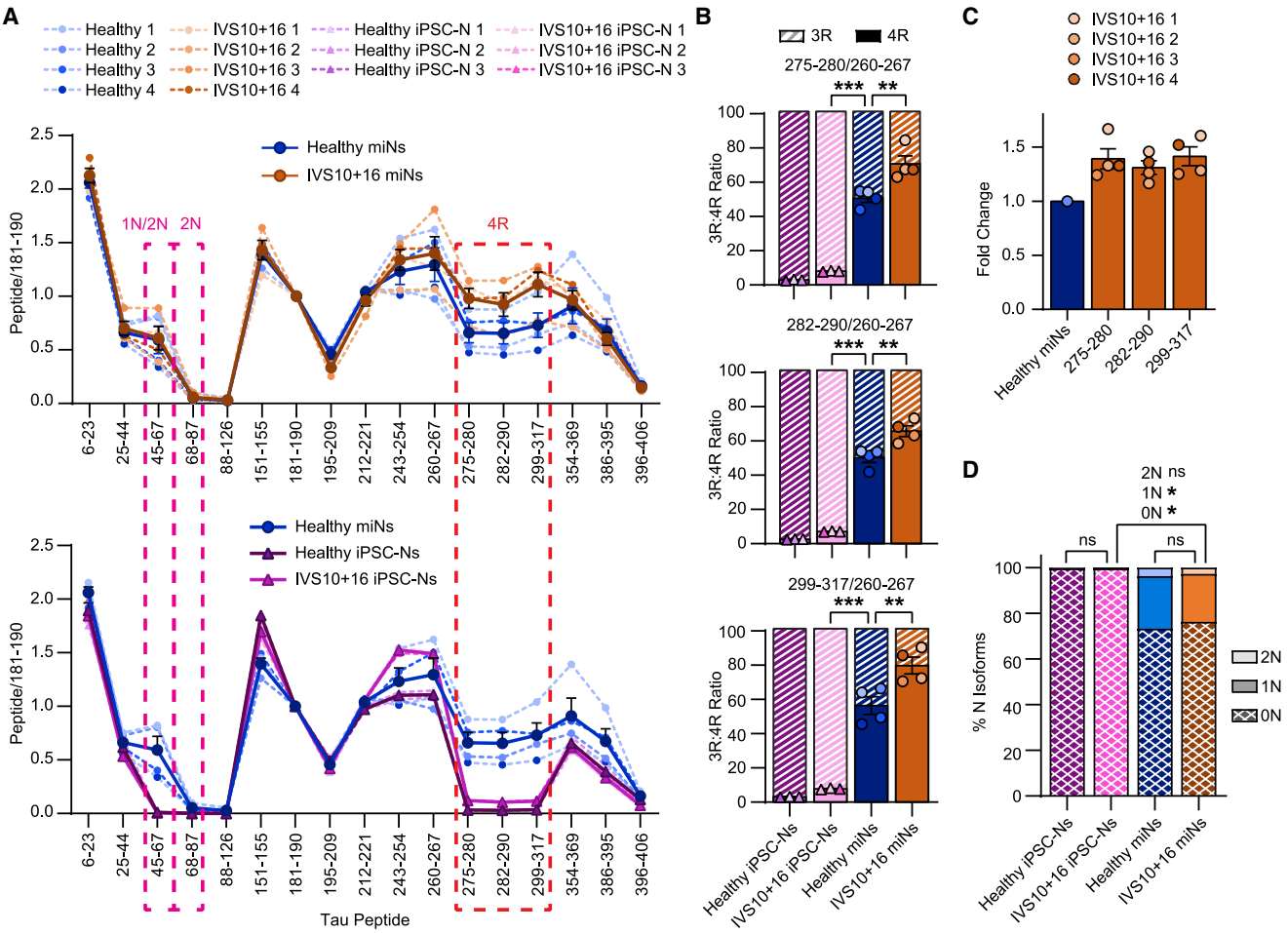

Figure 5. IVS10+16 patient-derived miNs demonstrate increased 4R protein corresponding to increased 4R mRNA

(A) Quantitation of relative tau peptides from multiple independent samples as indicated in the plot legend. Mean (thick line) ± SEM.

(B) Quantification of 3R:4R isoform ratio of all samples used in (A). Histogram colors are matched to sample colors shown in the plot legend of (A). Mean ± SEM. One-way ANOVA with multiple comparisons and post hoc Tukey's test; healthy miNs versus IVS10+16 miNs: 275–280 **p = 0.004, 282–290 **p = 0.004, and 299–317 **p = 0.008. Between any miN and iPSC-N: all peptides ***p $\leq$ 0.001.

(C) Fold change of 4R isoform expression using all healthy and IVS10+16 miNs in (A) for all three 4R-specific peptides over healthy miNs.

(D) Percentage of N isoforms using all samples as indicated in the plot legend in (A). Mean ± SEM; one-way ANOVA with multiple comparisons and post hoc Tukey's test. For all N isoforms: between healthy iPSC-Ns and IVS10+16 iPSC-Ns: ns p > 0.999; between healthy miNs versus IVS10+16 miNs: 0N: ns p = 0.97; 1N: ns p = 0.983; 2N: ns p = 0.887; between IVS10+16 miNs versus IVS10+16 iPSC-Ns: 0N: *p = 0.038; 1N: *p = 0.027; 2N: ns p = 0.285.

increase in 4R tau transcript whose expression becomes enhanced in 3D culturing condition (Choi et al., 2014; Kwak et al., 2020). Results shown here demonstrate miRNA-mediated neuronal conversion as a means to generate adult human neurons that mimic endogenous tau isoforms at both transcript and protein levels mirroring the 1-to-1 ratio of 3R:4R in the adult human brain. This ratio was strictly regulated in multiple independent donors. Using patient fibroblasts that harbor the IVS10+16 intronic mutation, we found that miRNA-reprogramming was sensitive to capture the difference in mRNA levels caused by the genetic mutation and the subsequent increase in 4R protein levels that reflect fold increase at mRNA level.

The directly converted human neuron model with robust 4R tau expression raises interesting future questions, for instance, which age-associated splicing factors drive exon 10 inclusion. Engineered mouse models expressing the entire human *MAPT* genomic sequence deviated from the expected 1:1 ratio of 3R:4R and showed a bias toward 3R (Duff et al., 2000), indicating there may exist splicing events and factors unique for 4R tau regulation in adult human neurons. Additionally, previous studies using tau minigenes to assay the regulation of tau exon 10 splicing in immortalized cell lines have implicated over 100 putative splicing effectors including SRSF7 (Cavaloc et al., 1994), SFPQ (Ishigaki et al., 2017), NOVA1 (Wang et al., 2004), and DYRK1A (Ding et al., 2012), but these remain to be validated in an adult human neuronal context that could be addressed using miNs.

The maintenance of age is required for modeling adult-onset disorders supported by recently published recent study of age-associated phenotypes in patient-derived neurons (Mertens et al., 2021; Victor et al., 2018). IVS10+16 patient-derived miNs

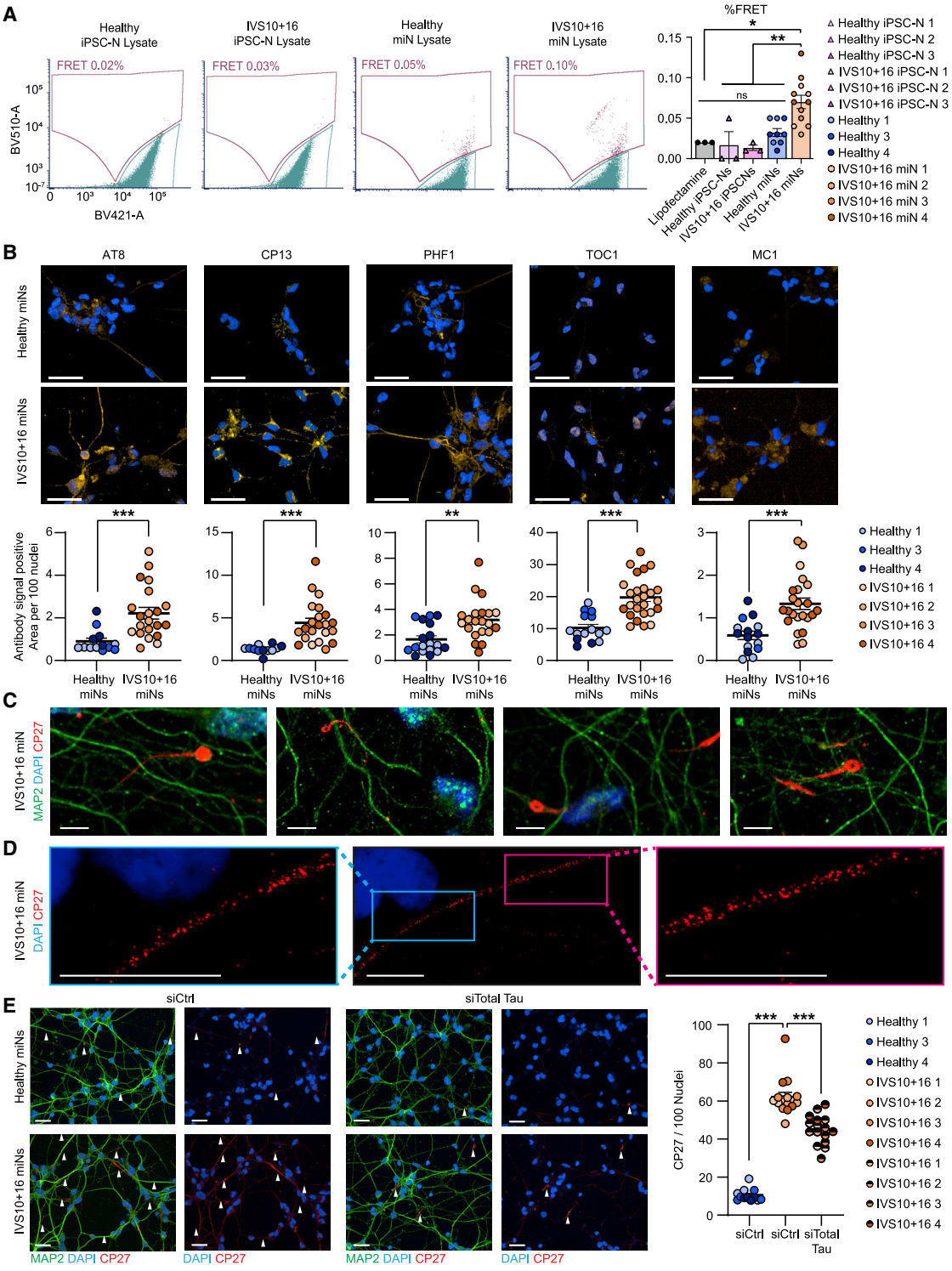

Figure 6. Formation of seed-capable and insoluble tau in IVS10+16 patient-derived miNs

(A) Left, representative FRET signals for healthy and IVS10+16 iPSC-N and miN lysate. Right, quantification of % FRET. n = 20,000 cells per FRET run. For iPSC-N samples, we performed three independent FRET runs per cell pellet. For miNs, we used three healthy and four IVS10+16 independent, individual samples, with three replicate FRET runs per sample. Mean ± SEM; one-way ANOVA with multiple comparisons. *p ≤ 0.05, **p ≤ 0.01.

(B) Top, representative images of methanol-fixed healthy and IVS10+16 miNs. Cells were colabeled with MAP2 antibody (green) and one of five anti-tau antibodies: AT8, CP13, PHF1, TOC1, and MC1 (yellow). Below, the quantification of anti-tau antibody signal positive area per 100 nuclei from three healthy and four IVS10+16 independent, individual samples as indicated in plot legend. Nuclei counted per condition: AT8: healthy miN = 70,939, IVS10+16 miN = 84,046;

(legend continued on next page)

develop increased insoluble tau inclusions and seed-competent tau, two defining characteristics of pathological tau from adult-onset tauopathy brains (Frost et al., 2009; Guo and Lee, 2011; Guo et al., 2016). The ability for a model to endogenously produce pathogenic tau will provide a system for assaying the prevention and clearing of insoluble tau. Of note, the model responded to the genetic knockdown of tau using siRNA that has therapeutic implications as antisense oligomer-directed reduction of tau is in human clinical trials (US National Library of Medicine, 2020).

Given the global increase in the aging population and the correlating increase in tauopathies, a model system that mirrors the adult human brain and its tau expression will provide an alternative avenue for studying these devastating diseases. The generation of human neurons that regulate tau splicing in the same way as the human adult brain and can replicate human tau-associated phenotypes represents a significant experimental advancement toward the investigation of tau-based pathology.

Limitations of the study

Although the data show that miNs provide an excellent model for studying tau isoform regulation and that they have the potential for testing pathological interventions in patient neurons, there is a limitation to direct reprogramming that should be noted. Scalability is limited due to tauopathy patient-derived fibroblasts being a rare commodity, especially those collected after symptom onset. This limitation highlights the need for more patient sample collection and availability to increase the scientific community's ability to leverage the benefit of direct neuronal conversion as an experimental system for adult-onset tauopathies.

STAR★METHODS

Detailed methods are provided in the online version of this paper and include the following:

- KEY RESOURCES TABLE
- RESOURCE AVAILABILITY
  - Lead contact
  - Materials availability
  - Data and code availability
- EXPERIMENTAL MODEL AND SUBJECT DETAILS
  - Fibroblast cell lines
  - Adult human brain samples
  - Fetal-aged human brain samples
  - Purchased iPSC-derived neuron samples
- METHOD DETAILS
  - Lentiviral production
  - Direct neuronal reprogramming
  - iPSC generation and genome engineering
  - iPSC differentiation
  - Immunocytochemistry
  - Quantitative PCR (qPCR)
  - Single-cell RNAseq sample preparation
  - 10x
  - Single-cell RNAseq data processing and analysis
  - Genotyping
  - RNAseq cell collection, sequencing, data processing, and analysis
  - Leafcutter data processing and analysis
  - Semi-quantitative PCR (sq-PCR)
  - Lysate Preparation for mass spectrometry analysis
  - Immunoprecipitation and mass spectrometry of tau isoforms
  - Immunoblot analysis
  - Biosensor cell culture methods
  - FRET flow cytometry
  - Immunocytochemistry, imaging and analysis
  - STED microscopy
  - SiRNA treatment of miNs
- QUANTIFICATION AND STATISTICAL ANALYSIS

SUPPLEMENTAL INFORMATION

Supplemental information can be found online at https://doi.org/10.1016/j.stem.2022.04.018.

ACKNOWLEDGMENTS

The authors would like to thank Edward D. Huey and Barbara Corneo (Columbia University) for providing one IVS10+16 fibroblast line, the Genome Technology Access Center and the fund from the Institute of Clinical and Translational Sciences (ICTS) (UL1TR002345) for their assistance in generating transcriptome dataset and iPSC lines, Mariana Beltcheva for iPSC-to-neuron differentiation, Kuo-Chan Weng for NPC expansion, Kitra Cates and Dr. Seongwon Lee for qPCR primers, Dr. Selina Wray for control and IVS10+16 iPSC-N lysate, Dr. Victoria Church for human brain miRNA, and Dr. Chloe He and Faris Shaikh for assisting with IP/MS experiments. This work was supported the following grants and awards: MCB training grant (T32 GM007067) (L.S.C.); ICTS JIT (JIT659H) (L.S.C. and A.S.Y.); Farrell Family Fund for Alzheimer's Disease (A.S.Y, C.M.K., and D.M.H.); Cure Alzheimer's Fund (A.S.Y.); NIH/NIA RF1AG056296 (A.S.Y.); NIH/NINDS R01NS107488 (A.S.Y.); Mallinckrodt Scholar Award (A.S.Y.); NIH/NIA K01AG062796 (C.S.); SILQ Center (R.J.B.); NIH/NINDS R01 NS095773 (R.J.B.); NIH/NIA AG063521 (K.E.D. and E.F.); the UK DRI funds from DRI Ltd, from the UK Medical Research Council, Alzheimer's Society, and Alzheimer's Research UK (K.E.D. and E.F.); MRC and Wellcome Trust (H.H.); NIH R56 NS110890 (C.M.K.); and Rainwater Charitable Organization (C.M.K.). ADRC Resources provided by Washington University Neuropathology core were supported by Healthy Aging and Senile Dementia (P01 AG03991), Alzheimer's Disease Research Center (P30 AG066444), Healthy Aging and Senile Dementia (P01

CP13: healthy miN = 69,708, IVS10+16 miN = 88,775; PHF1: healthy miN = 93,443, IVS10+16 miN = 71,070; TOC1: healthy miN = 47,280, IVS10+16 miN = 91,376; MC1: healthy miN = 94,171, IVS10+16 miN = 97,931. Scale bars, 50 μm.

(C) High magnification of methanol-fixed IVS10+16 miNs visualizing insoluble tau threads and tendrils stained with total tau antibody, CP27. Scale bars, 50 μm.

(D) Stimulated emission depletion (STED) microscopy of insoluble tau in IVS10+16 miNs. Scale bars, 10 μm.

(E) Left, arrowheads indicate the location of insoluble tau signals in healthy miNs (top) and IVS10+16 miNs (bottom). Left images: cells treated with control siRNA (siCtrl). Right images: cell treated with siRNA against total tau (siTotal tau). Right plot: quantification of tau signals detected per 100 nuclei (DAPI) in healthy miNs (healthy miNs treated with siCtrl) in comparison with IVS10+16 miNs treated with siCtrl and IVS10+16 miNs treated with siTotal tau from three healthy and four IVS10+16 independent, individual samples. Nuclei counted per condition: siCTRL on healthy miNs = 140,283; siCTRL on IVS10+16 miNs = 117,781; siTau on IVS10+16 miNs = 114,050. Mean ± SEM, one-way ANOVA with multiple comparisons. ***$p \leq 0.001$. Scale bars, 50 μm.

See also Figure S4.

AG03991), Alzheimer Disease Research Center (P50 AG05691), and the Adult Children Study (P01 AG026276).

AUTHOR CONTRIBUTIONS

Conceptualization, A.S.Y., D.M.H., K.E.D., and L.S.C.; methodology, A.S.Y. and L.S.C.; investigation, L.S.C., C.S., E.F., A.Y., K.H., J.-S.K., K.F.B., N.R.B., and S.G.F.; validation, A.S.Y. and S.G.F.; formal analysis, L.S.C.; writing – original draft, L.S.C. and A.S.Y.; writing – review and editing, all authors; supervision: R.J.B., R.I.M., K.E.D., and A.S.Y.

DECLARATION OF INTERESTS

D.M.H. is an inventor on a patent licensed by Washington University to C2N Diagnostics on the therapeutic use of anti-tau antibodies. D.M.H. cofounded and is on the scientific advisory board of C2N Diagnostics. C2N Diagnostics has licensed certain anti-tau antibodies to AbbVie for therapeutic development. D.M.H. is on the scientific advisory board of Denali, Genentech (South San Francisco, CA, USA), and Cajal Neurosciences and consults for Genentech, Takeda, Casma, and Eli Lilly. A.S.Y. consults for Roche. K.H. is an EISAI-sponsored visiting researcher at Washington University and has received salary from Eisai. K.E.D. is a board member and advisor for Ceracuity LLC. All other authors declare no competing interests.

Received: July 27, 2021
Revised: March 21, 2022
Accepted: April 27, 2022
Published: June 2, 2022

REFERENCES

Abernathy, D.G., Kim, W.K., McCoy, M.J., Lake, A.M., Ouwenga, R., Lee, S.W., Xing, X., Li, D., Lee, H.J., Heuckeroth, R.O., et al. (2017). MicroRNAs induce a permissive chromatin environment that enables neuronal subtype-specific reprogramming of adult human fibroblasts. Cell Stem Cell *21*, 332–348.e9. https://doi.org/10.1016/j.stem.2017.08.002.

Abernathy, D.G., and Yoo, A.S. (2015). MicroRNA-dependent genetic networks during neural development. Cell Tissue Res. *359*, 179–185. https://doi.org/10.1007/s00441-014-1899-4.

Abramoff, M., Magalhaes, P., and Ram, S. (2004). Image processing with ImageJ. Biophotonics international *11* (7), 36–42.

Andrews, S. (2010). FastQC: A Quality Control Tool for High Throughput Sequence Data [Online]. Available online at: http://www.bioinformatics.babraham.ac.uk/projects/fastqc/.

Antiabong, J.F., Ngoepe, M.G., and Abechi, A.S. (2016). Semi-quantitative digital analysis of polymerase chain reaction-electrophoresis gel: potential applications in low-income veterinary laboratories. Vet. World *9*, 935–939. https://doi.org/10.14202/vetworld.2016.935-939.

Barthélemy, N.R., Bateman, R.J., Hirtz, C., Marin, P., Becher, F., Sato, C., Gabelle, A., and Lehmann, S. (2020a). Cerebrospinal fluid phospho-tau T217 outperforms T181 as a biomarker for the differential diagnosis of Alzheimer's disease and PET amyloid-positive patient identification. Alzheimers Res. Ther. *12*, 26. https://doi.org/10.1186/s13195-020-00596-4.

Barthélemy, N.R., Li, Y., Joseph-Mathurin, N., Gordon, B.A., Hassenstab, J., Benzinger, T.L.S., Buckles, V., Fagan, A.M., Perrin, R.J., Goate, A.M., et al. (2020b). A soluble phosphorylated tau signature links tau, amyloid and the evolution of stages of dominantly inherited Alzheimer's disease. Nat. Med. *26*, 398–407. https://doi.org/10.1038/s41591-020-0781-z.

Beevers, J.E., Lai, M.C., Collins, E., Booth, H.D.E., Zambon, F., Parkkinen, L., Vowles, J., Cowley, S.A., Wade-Martins, R., and Caffrey, T.M. (2017). MAPT genetic variation and neuronal maturity alter isoform expression affecting axonal transport in iPSC-derived dopamine neurons. Stem Cell Rep. *9*, 587–599. https://doi.org/10.1016/j.stemcr.2017.06.005.

Braak, H., and Del Tredici, K. (2010). Neurofibrillary tangles. In Encyclopedia of Movement Disorders, K. Kompoliti and L.V. Metman, eds. (Academic Press), pp. 265–269. https://doi.org/10.1016/B978-0-12-374105-9.00269-0.

Cates, K., Mccoy, M.J., Kwon, J.S., Liu, Y., Abernathy, D.G., Zhang, B., Liu, S., Gontarz, P., Kim, W.K., Chen, S., et al. (2021). Deconstructing stepwise fate conversion of human fibroblasts to neurons by microRNAs. Cell Stem Cell *28*, 127–140.e9. https://doi.org/10.1016/j.stem.2020.08.015.

Cavaloc, Y., Popielarz, M., Fuchs, J.P., Gattoni, R., and Stévenin, J. (1994). Characterization and cloning of the human splicing factor 9G8: a novel 35 kDa factor of the serine/arginine protein family. EMBO J. *13*, 2639–2649. https://doi.org/10.1002/j.1460-2075.1994.tb06554.x.

Choi, S.H., Kim, Y.H., Hebisch, M., Sliwinski, C., Lee, S., D'Avanzo, C., Chen, H., Hooli, B., Asselin, C., Muffat, J., et al. (2014). A three-dimensional human neural cell culture model of Alzheimer's disease. Nature *515*, 274–278. https://doi.org/10.1038/nature13800.

Church, V.A., Cates, K., Capano, L., Aryal, S., Kim, W.K., and Yoo, A.S. (2021). Generation of human neurons by microRNA-mediated direct conversion of dermal fibroblasts. Methods Mol. Biol. *2239*, 77–100. https://doi.org/10.1007/978-1-0716-1084-8_6.

Clavaguera, F., Bolmont, T., Crowther, R.A., Abramowski, D., Frank, S., Probst, A., Fraser, G., Stalder, A.K., Beibel, M., Staufenbiel, M., et al. (2009). Transmission and spreading of tauopathy in transgenic mouse brain. Nat. Cell Biol. *11*, 909–913. https://doi.org/10.1038/ncb1901.

Connell, J.W., Rodriguez-Martin, T., Gibb, G.M., Kahn, N.M., Grierson, A.J., Hanger, D.P., Revesz, T., Lantos, P.L., Anderton, B.H., and Gallo, J.M. (2005). Quantitative analysis of tau isoform transcripts in sporadic tauopathies. Brain Res. Mol. Brain Res. *137*, 104–109. https://doi.org/10.1016/j.molbrainres.2005.02.014.

Ding, S., Shi, J., Qian, W., Iqbal, K., Grundke-Iqbal, I., Gong, C.-X., and Liu, F. (2012). Regulation of alternative splicing of tau exon 10 by 9G8 and Dyrk1A. Neurobiol. Aging *33*, 1389–1399. https://doi.org/10.1016/j.neurobiolaging.2010.11.021.

Dobin, A., and Gingeras, T.R. (2015). Mapping RNA-seq reads with STAR. Curr. Protoc. Bioinformatics *51*, 11.14.1–11.14.19. https://doi.org/10.1002/0471250953.bi1114s51.

Docagne, F., Nicole, O., Marti, H.H., Mackenzie, E.T., Buisson, A., and Vivien, D. (1999). Transforming growth factor-β1 as a regulator of the serpins/t-PA axis in cerebral ischemia. FASEB J. *13*, 1315–1324. https://doi.org/10.1096/fasebj.13.11.1315.

Duff, K., Knight, H., Refolo, L.M., Sanders, S., Yu, X., Picciano, M., Malester, B., Hutton, M., Adamson, J., Goedert, M., et al. (2000). Characterization of pathology in transgenic mice over-expressing human genomic and cDNA tau transgenes. Neurobiol. Dis. *7*, 87–98. https://doi.org/10.1006/nbdi.1999.0279.

Edgar, R., Domrachev, M., and Lash, A.E. (2002). Gene Expression Omnibus: NCBI gene expression and hybridization array data repository. Nucleic Acids Res. *30*, 207–210. https://doi.org/10.1093/nar/30.1.207.

Ehrlich, M., Hallmann, A.-L., Reinhardt, P., Araúzo-Bravo, M.J., Korr, S., Röpke, A., Psathaki, O.E., Ehling, P., Meuth, S.G., Oblak, A.L., et al. (2015). Distinct neurodegenerative changes in an induced pluripotent stem cell model of frontotemporal dementia linked to mutant Tau protein. Stem Cell Reports *5*, 83–96. https://doi.org/10.1016/j.stemcr.2015.06.001.

Frost, B., Jacks, R.L., and Diamond, M.I. (2009). Propagation of tau misfolding from the Outside to the inside of a cell. J. Biol. Chem. *284*, 12845–12852. https://doi.org/10.1074/jbc.M808759200.

Furman, J.L., Holmes, B.B., and Diamond, M.I. (2015). Sensitive detection of Proteopathic seeding activity with FRET flow cytometry. J. Vis. Exp. *106*, e53205. https://doi.org/10.3791/53205.

Gabel, H.W., Kinde, B., Stroud, H., Gilbert, C.S., Harmin, D.A., Kastan, N.R., Hemberg, M., Ebert, D.H., and Greenberg, M.E. (2015). Disruption of DNA-methylation-dependent long gene repression in Rett syndrome. Nature *522*, 89–93. https://doi.org/10.1038/nature14319.

Gamerdinger, M., Hajieva, P., Kaya, A.M., Wolfrum, U., Hartl, F.U., and Behl, C. (2009). Protein quality control during aging involves recruitment of the macroautophagy pathway by BAG3. EMBO J. *28*, 889–901. https://doi.org/10.1038/emboj.2009.29.

Gao, Y.-L., Wang, N., Sun, F.-R., Cao, X.-P., Zhang, W., and Yu, J.-T. (2018). Tau in neurodegenerative disease. Ann. Transl. Med. *6*, 175. https://doi.org/10.21037/atm.2018.04.23.

Ghetti, B., Oblak, A.L., Boeve, B.F., Johnson, K.A., Dickerson, B.C., and Goedert, M. (2015). Invited review: frontotemporal dementia caused by microtubule-associated protein tau gene (MAPT) mutations: a chameleon for neuropathology and neuroimaging. Neuropathol. Appl. Neurobiol. *41*, 24–46. https://doi.org/10.1111/nan.12213.

Goedert, M., and Jakes, R. (1990). Expression of separate isoforms of human Tau protein: correlation with the tau pattern in brain and effects on tubulin polymerization. EMBO J. *9*, 4225–4230. https://doi.org/10.1002/j.1460-2075.1990.tb07870.x.

Goedert, M., Spillantini, M.G., Jakes, R., Rutherford, D., and Crowther, R.A. (1989a). Multiple isoforms of human microtubule-associated protein tau: sequences and localization in neurofibrillary tangles of Alzheimer's disease. Neuron *3*, 519–526. https://doi.org/10.1016/0896-6273(89)90210-9.

Goedert, M., Spillantini, M.G., Potier, M.C., Ulrich, J., and Crowther, R.A. (1989b). Cloning and sequencing of the cDNA encoding an isoform of microtubule-associated protein tau containing four tandem repeats: differential expression of Tau protein mRNAs in human brain. EMBO J. *8*, 393–399.

Götz, J., Halliday, G., and Nisbet, R.M. (2019). Molecular pathogenesis of the tauopathies. Annu. Rev. Pathol. *14*, 239–261. https://doi.org/10.1146/annurev-pathmechdis-012418-012936.

Grover, A., Houlden, H., Baker, M., Adamson, J., Lewis, J., Prihar, G., Pickering-Brown, S., Duff, K., and Hutton, M. (1999). 5′ splice site mutations in tau associated with the inherited dementia FTDP-17 affect a stem-loop structure that regulates alternative splicing of exon 10. J. Biol. Chem. *274*, 15134–15143.

Guo, J.L., and Lee, V.M.-Y. (2011). Seeding of normal tau by pathological tau conformers drives pathogenesis of alzheimer-like tangles. J. Biol. Chem. *286*, 15317–15331. https://doi.org/10.1074/jbc.M110.209296.

Guo, J.L., Narasimhan, S., Changolkar, L., He, Z., Stieber, A., Zhang, B., Gathagan, R.J., Iba, M., McBride, J.D., Trojanowski, J.Q., and Lee, V.M.Y. (2016). Unique pathological tau conformers from Alzheimer's brains transmit tau pathology in nontransgenic mice. J. Exp. Med. *213*, 2635–2654. https://doi.org/10.1084/jem.20160833.

Ha, T.-Y., Choi, Y.R., Noh, H.R., Cha, S.-H., Kim, J.-B., and Park, S.M. (2021). Age-related increase in caveolin-1 expression facilitates cell-to-cell transmission of α-synuclein in neurons. Mol. Brain *14*, 122. https://doi.org/10.1186/s13041-021-00834-2.

He, Z., Mcbride, J.D., Xu, H., Changolkar, L., Kim, S.-J., Zhang, B., Narasimhan, S., Gibbons, G.S., Guo, J.L., Kozak, M., et al. (2020). Transmission of tauopathy strains is independent of their isoform composition. Nat. Commun. *11*, 7. https://doi.org/10.1038/s41467-019-13787-x.

Hefti, M.M., Farrell, K., Kim, S., Bowles, K.R., Fowkes, M.E., Raj, T., and Crary, J.F. (2018). High-resolution temporal and regional mapping of MAPT expression and splicing in human brain development. PLoS One *13*, e0195771. https://doi.org/10.1371/journal.pone.0195771.

Himmler, A., Drechsel, D., Kirschner, M.W., and Martin, D.W. (1989). Tau consists of a set of proteins with repeated C-terminal microtubule-binding domains and variable N-terminal domains. Mol. Cell. Biol. *9*, 1381–1388.

Holmes, B.B., Furman, J.L., Mahan, T.E., Yamasaki, T.R., Mirbaha, H., Eades, W.C., Belaygorod, L., Cairns, N.J., Holtzman, D.M., and Diamond, M.I. (2014). Proteopathic tau seeding predicts tauopathy in vivo. Proc. Natl. Acad. Sci. USA *111*, E4376–E4385. https://doi.org/10.1073/pnas.1411649111.

Horie, K., Barthélemy, N.R., Mallipeddi, N., Li, Y., Franklin, E.E., Perrin, R.J., Bateman, R.J., and Sato, C. (2020). Regional correlation of biochemical measures of amyloid and tau phosphorylation in the brain. Acta Neuropathol. Commun. *8*, 149. https://doi.org/10.1186/s40478-020-01019-z.

Huh, C.J., Zhang, B., Victor, M.B., Dahiya, S., Batista, L.F., Horvath, S., and Yoo, A.S. (2016). Maintenance of age in human neurons generated by microRNA-based neuronal conversion of fibroblasts. Elife *5*, e18648. https://doi.org/10.7554/eLife.18648.

Hutton, M., Lendon, C.L., Rizzu, P., Baker, M., Froelich, S., Houlden, H., Pickering-Brown, S., Chakraverty, S., Isaacs, A., Grover, A., et al. (1998). Association of missense and 5′-splice-site mutations in tau with the inherited dementia FTDP-17. Nature *393*, 702–705. https://doi.org/10.1038/31508.

Ishigaki, S., Fujioka, Y., Okada, Y., Riku, Y., Udagawa, T., Honda, D., Yokoi, S., Endo, K., Ikenaka, K., Takagi, S., et al. (2017). Altered tau isoform ratio caused by loss of FUS and SFPQ function leads to FTLD-like phenotypes. Cell Rep. *18*, 1118–1131. https://doi.org/10.1016/j.celrep.2017.01.013.

Jiang, S., Wen, N., Li, Z., Dube, U., Del Aguila, J., Budde, J., Martinez, R., Hsu, S., Fernandez, M.V., Cairns, N.J., et al. (2018). Integrative system biology analyses of CRISPR-edited iPSC-derived neurons and human brains reveal deficiencies of presynaptic signaling in FTLD and PSP. Transl. Psychiatry *8*, 265. https://doi.org/10.1038/s41398-018-0319-z.

Kang, M.-J., Chung, Y.H., Hwang, C.-I., Murata, M., Fujimoto, T., Mook-Jung, I.-H., Cha, C.I., and Park, W.-Y. (2006). Caveolin-1 upregulation in senescent neurons alters amyloid precursor protein processing. Exp. Mol. Med. *38*, 126–133. https://doi.org/10.1038/emm.2006.16.

Karch, C.M., Kao, A.W., Karydas, A., Onanuga, K., Martinez, R., Argouarch, A., Wang, C., Huang, C., Sohn, P.D., Bowles, K.R., et al. (2019). A comprehensive resource for induced pluripotent stem cells from patients with primary tauopathies. Stem Cell Rep. *13*, 939–955. https://doi.org/10.1016/j.stemcr.2019.09.006.

Kasai, N., Fukushima, K., Ueki, Y., Prasad, S., Nosakowski, J., Sugata, K.-I., Sugata, A., Nishizaki, K., Meyer, N.C., and Smith, R.J. (2001). Genomic structures of SCN2A and SCN3A – candidate genes for deafness at the DFNA16 locus. Gene *264*, 113–122. https://doi.org/10.1016/s0378-1119(00)00594-1.

Katsikoudi, A., Ficulle, E., Cavallini, A., Sharman, G., Guyot, A., Zagnoni, M., Eastwood, B.J., Hutton, M., and Bose, S. (2020). Quantitative propagation of assembled human Tau from Alzheimer's disease brain in microfluidic neuronal cultures. J. Biol. Chem. *295*, 13079–13093. https://doi.org/10.1074/jbc.RA120.013325.

King, I.F., Yandava, C.N., Mabb, A.M., Hsiao, J.S., Huang, H.-S., Pearson, B.L., Calabrese, J.M., Starmer, J., Parker, J.S., Magnuson, T., et al. (2013). Topoisomerases facilitate transcription of long genes linked to autism. Nature *501*, 58–62. https://doi.org/10.1038/nature12504.

Kosik, K.S., Orecchio, L.D., Bakalis, S., and Neve, R.L. (1989). Developmentally regulated expression of specific tau sequences. Neuron *2*, 1389–1397. https://doi.org/10.1016/0896-6273(89)90077-9.

Kovacs, G.G., and Gelpi, E. (2012). Clinical Neuropathology Practice News 3-2012: the "ABC" in AD – revised and updated guideline for the neuropathologic assessment of Alzheimer's disease. Clinical Neuropathology *31* (3), 116–118. https://doi.org/10.5414/NP300512.

Kwak, S.S., Washicosky, K.J., Brand, E., Von Maydell, D., Aronson, J., Kim, S., Capen, D.E., Cetinbas, M., Sadreyev, R., Ning, S., et al. (2020). Amyloid-β42/40 ratio drives tau pathology in 3D human neural cell culture models of Alzheimer's disease. Nat. Commun. *11*, 1377. https://doi.org/10.1038/s41467-020-15120-3.

Lapasset, L., Milhavet, O., Prieur, A., Besnard, E., Babled, A., Aït-Hamou, N., Leschik, J., Pellestor, F., Ramirez, J.-M., De Vos, J., et al. (2011). Rejuvenating senescent and centenarian human cells by reprogramming through the pluripotent state. Genes Dev. *25*, 2248–2253. https://doi.org/10.1101/gad.173922.111.

Lei, Z., Brizzee, C., and Johnson, G.V.W. (2015). BAG3 facilitates the clearance of endogenous tau in primary neurons. Neurobiol. Aging *36*, 241–248. https://doi.org/10.1016/j.neurobiolaging.2014.08.012.

Li, X., Zuo, X., Jing, J., Ma, Y., Wang, J., Liu, D., Zhu, J., Du, X., Xiong, L., Du, Y., et al. (2015). Small-molecule-driven direct reprogramming of mouse fibroblasts into functional neurons. Cell Stem Cell *17*, 195–203. https://doi.org/10.1016/j.stem.2015.06.003.

Li, H., Handsaker, B., Wysoker, A., Fennell, T., Ruan, J., Homer, N., Marth, G., Abecasis, G., and Durbin, R.; 1000 Genome Project Data Processing Subgroup (2009). The Sequence Alignment/Map format and SAMtools. Bioinformatics *25* (16), 2078–2079. https://doi.org/10.1093/bioinformatics/btp352.

Li, Y.I., Knowles, D.A., Humphrey, J., Barbeira, A.N., Dickinson, S.P., Im, H.K., and Pritchard, J.K. (2018). Annotation-free quantification of RNA splicing using LeafCutter. Nat. Genet. *50*, 151–158. https://doi.org/10.1038/s41588-017-0004-9.

Lim, L.P., Lau, N.C., Garrett-Engele, P., Grimson, A., Schelter, J.M., Castle, J., Bartel, D.P., Linsley, P.S., and Johnson, J.M. (2005). Microarray analysis shows that some microRNAs downregulate large numbers of target mRNAs. Nature *433*, 769–773. https://doi.org/10.1038/nature03315.

Liu, L., Drouet, V., Wu, J.W., Witter, M.P., Small, S.A., Clelland, C., and Duff, K. (2012). Trans-synaptic spread of tau pathology in vivo. PLoS One *7*, e31302. https://doi.org/10.1371/journal.pone.0031302.

Love, M.I., Huber, W., and Anders, S. (2014). Moderated estimation of fold change and dispersion for RNA-seq data with DESeq2. Genome Biol. *15*, 550. https://doi.org/10.1186/s13059-014-0550-8.

Lu, Y.-L., and Yoo, A.S. (2018). Mechanistic insights Into microRNA-induced neuronal reprogramming of human adult fibroblasts. Front. Neurosci. *12*, 522. https://doi.org/10.3389/fnins.2018.00522.

Maclean, B., Tomazela, D.M., Shulman, N., Chambers, M., Finney, G.L., Frewen, B., Kern, R., Tabb, D.L., Liebler, D.C., and MacCoss, M.J. (2010). Skyline: an open source document editor for creating and analyzing targeted proteomics experiments. Bioinformatics *26*, 966–968. https://doi.org/10.1093/bioinformatics/btq054.

Mahali, S., and Karch, C. (2021). Defective proteostasis in patient-derived iPSC-astrocytes and neurons carrying a MAPT IVS10+ 16 mutation. Alzheimers Dem. *17*, e058727.

Marone, M., Mozzetti, S., De Ritis, D., Pierelli, L., and Scambia, G. (2001). Semiquantitative RT-PCR analysis to assess the expression levels of multiple transcripts from the same sample. Biol. Proced. Online *3*, 19–25. https://doi.org/10.1251/bpo20.

Martin, M. (2011). Cutadapt removes adapter sequences from high-throughput sequencing reads. EMBnet.journal *17* (1), 10–12. https://doi.org/10.14806/ej.17.1.200.

Mazin, P., Xiong, J., Liu, X., Yan, Z., Zhang, X., Li, M., He, L., Somel, M., Yuan, Y., Phoebe Chen, Y.-P., et al. (2013). Widespread splicing changes in human brain development and aging. Mol. Syst. Biol. *9*, 633. https://doi.org/10.1038/msb.2012.67.

McCoy, M.J., Paul, A.J., Victor, M.B., Richner, M., Gabel, H.W., Gong, H., Yoo, A.S., and Ahn, T.-H. (2018). LONGO: an R package for interactive gene length dependent analysis for neuronal identity. Bioinformatics *34*, i422–i428. https://doi.org/10.1093/bioinformatics/bty243.

Mehra, A., Ali, C., Parcq, J., Vivien, D., and Docagne, F. (2016). The plasminogen activation system in neuroinflammation. Biochim. Biophys. Acta *1862*, 395–402. https://doi.org/10.1016/j.bbadis.2015.10.011.

Merry, D.E., Veis, D.J., Hickey, W.F., and Korsmeyer, S.J. (1994). bcl-2 protein expression is widespread in the developing nervous system and retained in the adult PNS. Development *120*, 301–311.

Mertens, J., Herdy, J.R., Traxler, L., Schafer, S.T., Schlachetzki, J.C.M., Böhnke, L., Reid, D.A., Lee, H., Zangwill, D., Fernandes, D.P., et al. (2021). Age-dependent instability of mature neuronal fate in induced neurons from Alzheimer's patients. Cell Stem Cell *28*, 1533–1548.e6. https://doi.org/10.1016/j.stem.2021.04.004.

Mertens, J., Paquola, A.C.M., Ku, M., Hatch, E., Böhnke, L., Ladjevardi, S., McGrath, S., Campbell, B., Lee, H., Herdy, J.R., et al. (2015). Directly reprogrammed human neurons retain aging-associated transcriptomic signatures and reveal age-related nucleocytoplasmic defects. Cell Stem Cell *17*, 705–718. https://doi.org/10.1016/j.stem.2015.09.001.

Patterson, M., Chan, D.N., Ha, I., Case, D., Cui, Y., Van Handel, B., Mikkola, H.K., and Lowry, W.E. (2012). Defining the nature of human pluripotent stem cell progeny. Cell Res. *22*, 178–193. https://doi.org/10.1038/cr.2011.133.

Ramírez, F., Dündar, F., Diehl, S., Grüning, B.A., and Manke, T. (2014). deepTools: a flexible platform for exploring deep-sequencing data. Nucleic Acids Research *42*, 187–191. https://doi.org/10.1093/nar/gku365.

Ramírez, F., Ryan, D.P., Grüning, B., Bhardwaj, V., Kilpert, F., Richter, A.S., Heyne, S., Dündar, F., and Manke, T. (2016). deepTools2: a next generation web server for deep-sequencing data analysis. Nucleic Acids Res. *44*, W160–W165. https://doi.org/10.1093/nar/gkw257.

Richner, M., Victor, M.B., Liu, Y., Abernathy, D., and Yoo, A.S. (2015). MicroRNA-based conversion of human fibroblasts into striatal medium spiny neurons. Nat. Protoc. *10*, 1543–1555. https://doi.org/10.1038/nprot.2015.102.

Satija, R., Farrell, J.A., Gennert, D., Schier, A.F., and Regev, A. (2015). Spatial reconstruction of single-cell gene expression data. Nat. Biotechnol. *33*, 495–502. https://doi.org/10.1038/nbt.3192.

Sato, C., Barthélemy, N.R., Mawuenyega, K.G., Patterson, B.W., Gordon, B.A., Jockel-Balsarotti, J., Sullivan, M., Crisp, M.J., Kasten, T., Kirmess, K.M., et al. (2018). Tau kinetics in neurons and the human central nervous system. Neuron *97*, 1284–1298.e7. https://doi.org/10.1016/j.neuron.2018.02.015.

Siahaan, V., Krattenmacher, J., Hyman, A.A., Diez, S., Hernández-Vega, A., Lansky, Z., and Braun, M. (2019). Kinetically distinct phases of tau on microtubules regulate kinesin motors and severing enzymes. Nat. Cell Biol. *21*, 1086–1092. https://doi.org/10.1038/s41556-019-0374-6.

Sposito, T., Preza, E., Mahoney, C.J., Setó-Salvia, N., Ryan, N.S., Morris, H.R., Arber, C., Devine, M.J., Houlden, H., Warner, T.T., et al. (2015). Developmental regulation of tau splicing is disrupted in stem cell-derived neurons from frontotemporal dementia patients with the 10 + 16 splice-site mutation in MAPT. Hum. Mol. Genet. *24*, 5260–5269. https://doi.org/10.1093/hmg/ddv246.

Sugino, K., Hempel, C.M., Okaty, B.W., Arnson, H.A., Kato, S., Dani, V.S., and Nelson, S.B. (2014). Cell-type-specific repression by methyl-CpG-binding Protein 2 is biased toward long genes. J. Neurosci. *34*, 12877–12883. https://doi.org/10.1523/JNEUROSCI.2674-14.2014.

Tan, R., Lam, A.J., Tan, T., Han, J., Nowakowski, D.W., Vershinin, M., Simó, S., Ori-McKenney, K.M., and McKenney, R.J. (2019). Microtubules gate tau condensation to spatially regulate microtubule functions. Nat. Cell Biol. *21*, 1078–1085. https://doi.org/10.1038/s41556-019-0375-5.

Tan, S.L., Ohtsuka, T., González, A., and Kageyama, R. (2012). MicroRNA9 regulates neural stem cell differentiation by controlling Hes1 expression dynamics in the developing brain. Genes Cells *17*, 952–961. https://doi.org/10.1111/gtc.12009.

Tanner, M.K., Tang, Z., and Thornton, C.A. (2021). Targeted splice sequencing reveals RNA toxicity and therapeutic response in myotonic dystrophy. Nucleic Acids Res. *49*, 2240–2254. https://doi.org/10.1093/nar/gkab022.

Thompson, C.H., Ben-Shalom, R., Bender, K.J., and George, A.L. (2020). Alternative splicing potentiates dysfunction of early-onset epileptic encephalopathy SCN2A variants. J. Gen. Physiol. *152*. https://doi.org/10.1085/jgp.201912442.

Thorvaldsdóttir, H., Robinson, J.T., and Mesirov, J. (2013). Integrative Genomics Viewer (IGV): high-performance genomics data visualization and exploration. Brief Bioinformatics *14* (2), 178–192. https://doi.org/10.1093/bib/bbs01.

US National Library of Medicine (2020). Safety, tolerability and pharmacokinetics of multiple ascending doses of NIO752 in progressive supranuclear palsy. US National Library of Medicine. https://ClinicalTrials.gov/show/NCT04539041.

Verheyen, A., Diels, A., Dijkmans, J., Oyelami, T., Meneghello, G., Mertens, L., Versweyveld, S., Borgers, M., Buist, A., Peeters, P., and Cik, M. (2015). Using human iPSC-derived neurons to model TAU aggregation. PLoS One *10*, e0146127. https://doi.org/10.1371/journal.pone.0146127.

Verheyen, A., Diels, A., Reumers, J., Van Hoorde, K., Van den Wyngaert, I., van Outryve d'Ydewalle, C., De Bondt, A., Kuijlaars, J., De Muynck, L., De Hoogt, R., et al. (2018). Genetically engineered iPSC-derived FTDP-17 MAPT neurons display mutation-specific neurodegenerative and neurodevelopmental phenotypes. Stem Cell Reports *11*, 363–379. https://doi.org/10.1016/j.stemcr.2018.06.022.

Victor, M.B., Richner, M., Hermanstyne, T.O., Ransdell, J.L., Sobieski, C., Deng, P.-Y., Klyachko, V.A., Nerbonne, J.M., and Yoo, A.S. (2014). Generation of human striatal neurons by microRNA-dependent direct conversion of fibroblasts. Neuron *84*, 311–323. https://doi.org/10.1016/j.neuron.2014.10.016.

Victor, M.B., Richner, M., Olsen, H.E., Lee, S.W., Monteys, A.M., Ma, C., Huh, C.J., Zhang, B., Davidson, B.L., Yang, X.W., and Yoo, A.S. (2018). Striatal neurons directly converted from Huntington's disease patient fibroblasts recapitulate age-associated disease phenotypes. Nat. Neurosci. *21*, 341–352. https://doi.org/10.1038/s41593-018-0075-7.

Wang, J., Gao, Q.-S., Wang, Y., Lafyatis, R., Stamm, S., and Andreadis, A. (2004). Tau exon 10, whose missplicing causes frontotemporal dementia, is regulated by an intricate interplay of cis elements and trans factors. J. Neurochem. *88*, 1078–1090. https://doi.org/10.1046/j.1471-4159.2003.02232.x.

Yoo, A.S., Staahl, B.T., Chen, L., and Crabtree, G.R. (2009). MicroRNA-mediated switching of chromatin-remodelling complexes in neural development. Nature *460*, 642–646. https://doi.org/10.1038/nature08139.

Yoo, A.S., Sun, A.X., Li, L., Shcheglovitov, A., Portmann, T., Li, Y., Lee-Messer, C., Dolmetsch, R.E., Tsien, R.W., and Crabtree, G.R. (2011). MicroRNA-mediated conversion of human fibroblasts to neurons. Nature *476*, 228–231. https://doi.org/10.1038/nature10323.

Zerbino, D.R., Johnson, N., Juettemann, T., Wilder, S.P., and Flicek, P. (2014). WiggleTools: parallel processing of large collections of genome-wide datasets for visualization and statistical analysis. Bioinformatics *30* (7), 1008–1009. https://doi.org/10.1093/bioinformatics/btt737.

Zhao, C., Sun, G., Li, S., and Shi, Y. (2009). A feedback regulatory loop involving microRNA-9 and nuclear receptor TLX in neural stem cell fate determination. Nat. Struct. Mol. Biol. *16*, 365–371. https://doi.org/10.1038/nsmb.1576.

Zheng, G.X.Y., Terry, J.M., Belgrader, P., Ryvkin, P., Bent, Z.W., Wilson, R., Ziraldo, S.B., Wheeler, T.D., McDermott, G.P., Zhu, J., et al. (2017). Massively parallel digital transcriptional profiling of single cells. Nat. Commun. *8*, 14049. https://doi.org/10.1038/ncomms14049.

STAR★METHODS

KEY RESOURCES TABLE

REAGENT or RESOURCE	SOURCE	IDENTIFIER
Antibodies		
Rabbit polyclonal anti-MAP2	Cell Signaling Technology	Cat# 4542S; RRID: AB_ 10693782
Rabbit polyclonal anti-MAP2	Millipore	Cat# AB5622; RRID: AB_91939
Rabbit polyclonal anti-Tau	Aligent/Dako	Cat# 002401-2; RRID: AB_10013724
Mouse monoclonal anti-TUBB3	BioLegend	Cat# 801202; RRID: AB_ 10063408
Rabbit polyclonal anti-TUBB3	BioLegend	Cat# 802001, RRID: AB_2564645
Chicken polyclonal anti-TUBB3	Novus	Cat# NB100-1612, RRID: AB_10000548
Mouse monoclonal anti-Tau (CP-27)	Peter Davies, Albert Einstein College of Medicine	Cat# CP-27; RRID: AB_2716722
Mouse monoclonal anti-Tau (Tau1)	Nicholas M. Kanaan, Michigan State University	Cat# Tau1; RRID: AB_2721197
Mouse monoclonal anti-Tau (HJ8.5)	David Holtzman, Washington University in St. Louis	Cat# HJ8.5; RRID: AB_2721237
Mouse monoclonal anti-NCAM1	Santa Cruz Biotechnology	Cat#SC-106; RRID: AB_627128
Mouse monoclonal anti-pTau (AT8)	Thermo Fisher Scientific	Cat# MN1020; RRID: AB_223647
Mouse monoclonal anti-pTau (CP13)	Peter Davies, Albert Einstein College of Medicine	Cat# CP13; RRID: AB_2314223
Mouse monoclonal anti-conformationally abnormal Tau (MC1)	Peter Davies, Albert Einstein College of Medicine	Cat# MC1; RRID: AB_2314773
Mouse monoclonal anti-pTau (PHF1)	Peter Davies, Albert Einstein College of Medicine	Cat# PHF1; RRID: AB_2315150
Mouse monoclonal anti-oligomeric Tau (TOC1)	Nicholas M. Kanaan, Michigan State University	Cat# TOC1; RRID: AB_2832939
Rabbit polyclonal anti-Neurofilament Heavy Chain	Abcam	Cat# ab8135; RRID: AB_306298
Abberior StarRed goat anti-mouse	Abberior	Cat# STRED-1001-500UG
Biological samples		
Fetal Brain RNA– Fbrain 1	Tebu Bio	1F01-50
Fetal Primary Neurons – FPN 1	ScienCell	1520
Fetal Primary Neurons – FPN 2	ScienCell	1520
Fetal Primary Neurons – FPN 3	ScienCell	1520
iPSC-derived cortical neurons – iPSC-CN 1	BrainXell	BX-0300
Fetal neuron lysate – FNL 1	ScienCell	1526
Adult Brain RNA, Male 29yr - ABrain 1	BioChain	R1234066-50
Adult Brain RNA, Male 66yr - ABrain 2	BioChain	R1234066-50
Adult Brain RNA, Female 78yr - ABrain 3	BioChain	R1234066-50
Adult Brain RNA, Male 82yr - ABrain 4	NovusBio	NB820-59177
Adult Brain Lysate, Male 90yrs - ABrain 5	Dr. Chihiro Sato, Washington University in Saint Louis	n/a
Adult Brain Lysate, Male 80yrs - ABrain 6	Dr. Chihiro Sato, Washington University in Saint Louis	n/a
Adult Brain Lysate, Male 87yrs - ABrain 7	Dr. Chihiro Sato, Washington University in Saint Louis	n/a
Adult Brain Lysate, Male 72yrs - ABrain 8	Dr. Chihiro Sato, Washington University in Saint Louis	n/a
IVS10+16 Adult Brain RNA, Male 66rs – IVS10+16 ABrain	Queen Square House Brain Bank	P2/08

(*Continued on next page*)

Continued

REAGENT or RESOURCE	SOURCE	IDENTIFIER
Chemicals, peptides, and recombinant proteins		
Fetal bovine serum (FBS), qualified, US Department of Agriculture (USDA)-approved regions	Life Technologies	Cat# 10437028
Polybrene	Sigma-Aldrich	Cat# H9268
Neurobasal-A	Gibco	Cat# 10888022
GlutaMAX	Gibco	Cat# 35050061
B27 Plus Supplement	Gibco	Cat# A3582801
BrainPhys Neuronal Medium	StemCell	Cat# 05790
NeuroCult SM1 Neuronal Supplement	StemCell	Cat# 05711
N2 Supplement-A	StemCell	Cat# 07152
Doxycycline hyclate (Dox)	Sigma-Aldrich	Cat# D9891
Poly-L-ornithine solution	Sigma-Aldrich	Cat# P4957
Laminin	Sigma-Aldrich	Cat# L2020
Fibronectin	Sigma-Aldrich	Cat# F4759
Valproic acid (VPA), sodium salt	Sigma-Aldrich	Cat# 676380
Dibutyryl-cAMP sodium salt	Sigma-Aldrich	Cat# D0627
Retinoic acid (RA)	Sigma-Aldrich	Cat# R2625
Neurotrophin-3 (NT-3)	PeproTech	Cat# 450-03
Brain-derived neurotrophic factor (BDNF)	PeproTech	Cat# 450-02
Glial-derived Neurotrophic Factor (GDNF)	PeproTech	Cat# 450-10
RevitaCell Supplement	Thermo Fisher Scientific	Cat# A2644501
ISX-9	StemCell Technologies	Cat# 73202
DAPT	Millipore Sigma	Cat# D5942
Critical commercial assays		
Go Taq DNA Polymerase	Promega	Cat# M3001
RNeasy Plus Micro Kit	QIAGEN	Cat# 74034
SMARTer Ultra Low RNA Kit for Illumina sequencing	Clontech	Cat# 635029
TruSeq Small RNA Library Preparation Kit	Illumina	Cat# RS-200-0012
ReliaPrep™ RNA Miniprep Systems	Promega	Cat# Z6011
QIAamp DNA Mini Kit	QIAGEN	Cat# 51304
QIAquick Gel Extraction Kit	QIAGEN	Cat# 28706
Deposited data		
Raw and processed data (Single-cell RNA-sequencing, bulk RNA-sequencing)	NCBI Gene Expression Omnibus (Edgar et al., 2002)	GEO: GSE201084
Western Blot	Mendeley Data	Mendeley Data: https://doi.org/10.17632/t93byrznm6.1
Experimental models: Cell lines		
Lenti-X 293LE cell line	Clontech	Cat# 632180
AG04148, Male 56yrs – Control 1	Coriell	Cat# AG04148
AG08260, Male 61yrs – Control 2	Coriell	Cat# AG08260
AG08379, Female 60yrs – Control 3	Coriell	Cat# AG08379
AG13369, Male 68yrs – Control 4	Coriell	Cat# AG13369
UCL455, Male 53yrs – IVS10+16 1	Dr.Henry Houlden, University College London	n/a
UCL457, Male 52yrs – IVS10+16 2	Dr.Henry Houlden, University College London	n/a

(*Continued on next page*)

Continued

REAGENT or RESOURCE	SOURCE	IDENTIFIER
UCL497, Female 54yrs – IVS10+16 3	Dr.Henry Houlden, University College London	n/a
ES046, Male 57yrs – IVS10+16 4	Dr. Barbara Corneo, Columbia University	n/a
Oligonucleotides		
Primers for qPCR; see Table S3	This paper	n/a
Primers for sqPCR; see Table S3	This paper	n/a
Primers for sequencing; see Table S3	This paper	n/a
Recombinant DNA		
pMD2.G	Didier Trono	12259
psPAX2	Didier Trono	12260
rtTA-N144	Richner et al., 2015	66810
pTight-9/9*-124-BclxI	Victor et al., 2014	60857
MYT1L-N174	Richner et al., 2015	66809
Software and algorithms		
ImageJ	Abramoff et al., 2004	https://imagej.nih.gov/ij/
LAS X	Leica Microsystems	https://www.leica-microsystems.com/products/microscope-software/p/leica-las-x-ls/
Harmony v4.9	Perkin Elmer	https://www.perkinelmer.com/product/harmony-4-8-office-hh17000001
Graphpad Prism 9	GraphPad Software Inc	http://www.graphpad.com/
FCS Express 7 Research software	De Novo Software	https://denovosoftware.com/
Ingenuity Pathway Analysis	QIAGEN	https://digitalinsights.qiagen.com/products-overview/discovery-insights-portfolio/analysis-and-visualization/qiagen-ipa/
Skyline	MacCoss Lab Software, MacLean et al., 2010	https://skyline.ms/project/home/software/Skyline/begin.view
Cell Ranger (v3.1.0)	10x Genomics, Zheng et al., 2017	https://support.10xgenomics.com/single-cell-gene-expression/software/pipelines/latest/what-is-cell-ranger
Seurat (v3.2.3)	Santija Lab, Satija et al., 2015	https://satijalab.org/seurat/
Cutadapt v2.4	Martin, 2011; National Bioinformatics Infrastructure Sweden	https://github.com/marcelm/cutadapt/
DESeq2	Love et al., 2014	https://bioconductor.org/packages/release/bioc/html/DESeq2.html
FastQC v0.11.4	FastQC: A Quality Control Tool for High Throughput Sequence Data	https://www.bioinformatics.babraham.ac.uk/projects/fastqc/
Deeptools (v3.5.1)	Ramírez et al., 2014	http://deeptools.ie-freiburg.mpg.de
Wiggletools (v1.2)	Zerbino et al., 2014	www.github.com/Ensembl/Wiggletools
Samtools v1.9	Li et al., 2009	http://samtools.sourceforge.net/
Picard v2.18	Broad Institute	https://broadinstitute.github.io/picard/
IGV	Thorvaldsdóttir et al., 2013	https://software.broadinstitute.org/software/igv/download
STAR	Dobin et al., 2015	https://github.com/alexdobin/STAR
LONGO	McCoy et al., 2018	https://github.com/biohpc/longo
Leafcutter	Li et al., 2018	https://davidaknowles.github.io/leafcutter/

RESOURCE AVAILABILITY

Lead contact

Further information and requests for reagents should be directed to and will be fulfilled by the Lead Contact, Andrew S. Yoo (yooa@wustl.edu).

Materials availability

All unique and stable reagents generated in this study are available from the Lead Contact with a completed Materials Transfer Agreement.

Data and code availability

- Single-cell and bulk RNA-seq data have been deposited at GEO and are publicly available as of the date of publication. Accession numbers are listed in the key resources table. Original western blot images have been deposited at Mendeley and are publicly available as of the date of publication. The DOI is listed in the key resources table.
- This paper does not report original code.
- Any additional information required to reanalyze the data reported in this work paper is available from the Lead Contact upon request.

EXPERIMENTAL MODEL AND SUBJECT DETAILS

Fibroblast cell lines

Healthy human fibroblasts were obtained from Coriell NINDS (AG04148 – Male 56yrs, AG08260 – Male 61yrs, AG08379 – Female 60yrs, and AG13369 – Male 68yrs) while IVS10+16 patient fibroblasts were acquired from Columbia University (ES046 – Male 57yrs) and University College London (UCL455 – Male 53yrs, UCL457 – Male 52yrs, and UCL497 – Female 54yrs). All fibroblasts were maintained in DMEM with 15% FBS for growth. We do not have access to original patient data, and therefore cannot identify the donor. The research falls outside the federal definition under the jurisdiction of an institutional review board and is exempt from human subject studies. Samples were grouped by *MAPT* genotype.

Adult human brain samples

Three biological replicate lots of adult human brain RNA (R1234066-50) (Lot C.210018 – ABrain1 Male 29yrs, Lot B.210080 – ABrain2 Male 66yrs, Lot B.811107 – ABrain3 Female 78yrs) was purchased from BioChain. Adult human brain protein samples include Novus purchased lysate (NB820-59177) (Lot C.111050 – ABrain4 Male 82yrs) and four previously published healthy samples (Lot 61732 – ABrain5 Male 90yrs, Lot 65241 – ABrain6 Male 80yrs, Lot 65318 – ABrain7 Male 87yrs, Lot 84868 – ABrain8 Male 72yrs) obtained from Washington University Alzheimer's Disease Research Center (ADRC) (Horie et al., 2020). All participants were between A0B1 and A3B1 on the ABC Alzheimer's Disease lesion scoring system (Kovacs and Gelpi, 2012) (none had clinical symptoms and they were not diagnosed with Alzheimer's Disease). The study was approved by the Washington University Institutional Review Board, and all participants were purchased from BrainXell (#BX-0300). IVS10+16 human brain (P2/08) from Queen Square House Brain Bank. Samples were grouped by *MAPT* genotype.

Fetal-aged human brain samples

Fetal human brain RNA (#1F01-50) (Lot 1333 – Fbrain1 Male 21weeks) was purchased from Cell Applications Inc. Fetal human neuron lysate (#1526) (Lot 2219 – FNL1 sex and age not available) was purchased from ScienCell. Primary fetal neurons (#1520) (Lot 29207 – FPN1 sex unknown 19wks post-conception, Lot 28630 – FPN2 Male 22wks post conception, Lot 29390 – FPN3 Male 18wks post-conception) were purchased from ScienCell and were thawed and cultured in Neuronal Medium (ScienCell #1521). Samples were grouped by cellular age.

Purchased iPSC-derived neuron samples

For bulk and single cell RNA-sequencing and sqPCR, differentiated iPSC-derived Cortical Glutamatergic Neurons (Lot 200107 – iPSC-CN1 Female) were purchased from BrainXell (#BX-0300) and cultured according to BrainXell protocol in DMEM with F12 and additional neuronal supplements. Samples were grouped by cellular age.

METHOD DETAILS

Lentiviral production

Lentiviruses were generated as previously described (Church et al., 2021) with minor changes. To make supernatant virus, viral supernatant was collected, spun at 1200g for 5min at 4°C, then passed through a 0.45uM filter. This supernatant was then aliquoted and directly frozen at -80°C until used (less than 1 year after production date).

Direct neuronal reprogramming

Human fibroblasts were directly reprogrammed to miNs as previously described (Church et al., 2021; Richner et al., 2015; Yoo et al., 2011) with slight modification. Briefly, fibroblasts were transduced with supernatant lentivirus mix comprised of dox-inducible miR-9/9*-124, rtTA, and the transcription factor MYT1L. From PID1 to PID14 cells were treated with DAPT (2uM) to increase neurite outgrowth and neuronal differentiation, and on PID 3, 6, 10, and 14, cells were also treated with the NEUROD1-activator ISX9 (10uM) to push cortical fate. Fibroblasts and reprogramming cells were cultured in DMEM+10%FBS through replating at PID5.

On PID6, cells were switched to Neurobasal-A with B27+ (1000x) and Glutamax (500x), containing 1 μg/mL doxycycline, 200 μM dibutyl cyclic AMP, 1 mM valproic acid, 2uM DAPT, 200nM Ascorbic Acid, 10 ng/mL BDNF, 10 ng/mL NT-3, 1 μM retinoic acid, 10uM ISX9, 100x RVC, and 3 μg/mL puromycin. Cells were half fed every 4 days and doxed every 4 days on an offsetting 2 day scheduled. On PID14, miNs were half fed using BrainPhys containing N2A and SM1 (StemCell) with the following goodies: 1 μg/mL doxycycline, 200 μM dibutyl cyclic AMP, 1 mM valproic acid, 2uM DAPT, 200nM Ascorbic Acid, 10 ng/mL BDNF, 10 ng/mL NT-3, and 1 μM retinoic acid.

iPSC generation and genome engineering

Dermal fibroblasts from MAPT IVS10+16 carriers (GIH36) were transduced with nonintegrating Sendai virus carrying OCT3/4, SOX2, KLF4, and cMYC (Life Technologies) as previously described (Karch et al., 2019). iPSC that were heterozygous for MAPT IVS10+16 were edited to WT (GIH36.2Δ1D01) using CRISPR/Cas9 as previously reported (Karch et al., 2019). Mutation status was confirmed by Sanger sequencing. Cell lines were maintained in mTesR medium (StemCell Technologies) on Matrigel. Cell lines were confirmed to be free of mycoplasma.

iPSC differentiation

MAPT IVS10+16 iPSC (n=1) and isogenic controls (n=1) were differentiated into neural progenitor cells (NPCs) as previously described (Jiang et al., 2018; Karch et al., 2019). Briefly, iPSC were dissociated with Accutase (Life Technologies). iPSCs were then plated at 65,000 cells per well in Neural Induction Media (NIM; Stem Cell Technologies) in a 96-well v-bottom plate to form neural aggregates. After 5 days, neural aggregates were plated on Poly-L-Ornithine (PLO) and laminin-coated plates to form neural rosettes. After 5 to 7 days, neural rosettes were isolated by enzymatic selection and cultured as NPCs. NPCs were cultured on PLO and laminin-coated plates and terminal differentiation was initiated with the addition of cortical maturation medium (Neurobasal-A (Life Technologies) supplemented with 1x B27 (Gibco), 20ng/mL BDNF (Peprotech), 20ng/mL GDNF (Peprotech), 0.5mM cAMP (Sigma) and 1% L-glutamate (Sigma)). Neural cultures were maintained for six weeks.

Immunocytochemistry

Cells are fixed with either 4% PFA for 20min and washed 3x PBS after fixation. Fixed cells were permeabilized for 10min at RT in permeabilization buffer, blocked for 1hr RT in 5% BSA/1% NGS, then stained in primary antibody in blocking buffer overnight 4°C. The next day, cells were washed 3x in PBS and placed in secondary antibody 1:1000 in blocking buffer for 1hr room temp. Cells were washed 3x in PBS and stained with DAPI for 10min RT, washed once with PBS, then mounted in ProLong Gold antifade Mountant. Primary antibodies used for the immunofluorescence imaging: mouse anti-NCAM (Santa Cruz, SC-106 1:50), rab anti-Tau (Aligent/DAKO, A002401-2 1:200), rab anti-TUBB3 (Biolegend, 802001 1:2000), mouse anti-TUBB3 (Biolegend, 801202 1:2000), chicken anti-TUBB3 (Novus, NB100-1612 1:1000), mouse anti-tau (CP27) (generously provided by Dr. Peter Davies, 1:400), mouse anti-pTau (PHF1) (generously provided by Dr. Peter Davies, 1:1000), mouse anti-pTau (AT8) (Invitrogen, MN1020, 1:1000), mouse anti-pTau (CP13) (generously provided by Dr. Peter Davies, 1:500), mouse anti-Tau (MC1) (generously provided by Dr. Peter Davies, 1:500), mouse anti-Tau (TOC1) (generously provided by Dr. Nicholas Kanaan, 1:500), rabbit anti-MAP2 (Cell Signaling, #4542 1:200), rabbit anti-MAP2 (Millipore, AB5622 1:1000), The secondary antibodies were goat anti-mouse, -rabbit, or -chicked IgG conjugated with Alexa-488, Alexa-594, or Alexa-647 (Invitrogen).

Immunostained images were taken using a Leica SP5X white light laser confocal system with Leica Application Suite (LAS) Advanced Fluorescence 2.7.3.9723. All antibodies were validated for functionality through negative control screening of fibroblasts. Composite images were stitched during acquisition in LAS software.

Quantification of cell fate immunocytochemistry was performed using imageJ multi tool counter. Intact nuclei were used to count total cells, and MAP2 and tau positive cells were defined by the presence of two or more fluorescent-positive neurites whose length is twice the size of the soma. N represents the total number of live cells counted per cell line, as outlined in figure legends. Percentages were calculated in Excel.

Quantitative PCR (qPCR)

Total RNA was extracted from miNs using TRIzol (Invitrogen, USA) following manufacturer protocol. Reverse-transcription was performed with 150-200ng of RNA with SuperScript IV First Strand Synthesis SuperMix (Invitrogen, USA). qPCR assay was run with SYBR Green PCR Master Mix and plate was run and analyzed on StepOnePlus Real-Time PCR System (AB Applied Biosystems, Germany). Each sample was run in triplicate and the mean of each sample is represented as a single data point. Expression values were calculated in Excel using the delta Ct method and Z-score calculation.

Single-cell RNAseq sample preparation

Reprogrammed cells, fibroblasts, and cultured iPSC-Ns were collected as previously published (Cates et al., 2021). Briefly, cells were washed once with 1xDPBS, 200μL of 0.25% trypsin was added to the wells and plates were placed at 37°C for 5 minutes. Wells were flooded with 500μL warm 10% DMEM. Cells were collected in a 5mL Eppendorf and centrifuged at 300g for 5 minutes at 37°C. Supernatant was removed and the pellet was resuspended in 0.04% BSA in PBS and spun again. Pellet was resuspended in 0.04% BSA in PBS, cells were counted on a hemocytometer, and volume was adjusted to achieve 1,000 cells/μL. All samples were placed on ice and immediately brought to the Genome Technology Access Center at Washington University in Saint Louis (https://gtac.wustl.edu/).

10x

Single-cell RNAseq was performed on the 10x Genomics platform, using the Chromium Single Cell 3' kits: Library & Gel Bead Kit v2 (PN-120237), Chip kit v2 (PN-120236), and i7 Multiplex Kit (PN-120262), following manufacturer-provided user guide. Agilent Bioanalyzer was used for cDNA library quantification.

Single-cell RNAseq data processing and analysis

The raw 10x reads were processed with the Cell Ranger count pipeline using default parameters (Cell Ranger v3.1.0, 10x Genomics. Reads were aligned to the hg38 reference index provided by 10x Genomics (refdata-cellranger-GRCh38 v3.0.0). Cell barcode and unique molecular identifier (UMI) were extracted and corrected from the feature library using the same methods as gene expression read processing. Feature-barcode matrices were generated by counting distinct UMIs of each gene within a given individual cell (Zheng et al., 2017).

The R package, Seurat (v3.2.3) was used for quality control, analysis, and exploration of scRNA-seq data (Satija et al., 2015). We first removed cells where features less than 200 were detected and mitochondrial counts were high, then filtered features detected in cells less than 10. Seurat was used to remove unwanted variation from the gene expression by regressing out proportion of mitochondrial UMIs and overall UMIs. Highly variable genes were identified and used as input for dimensionality reduction via Principal Component Analysis (PCA). The resulting PCs and the correlated genes were examined to determine the number of components to be included in downstream analysis. These principal components were then used as inputs to cluster individual cells, using a K-nearest neighbor graph and the Louvain algorithm. The resulting cell clusters were visualized and explored using UMAP as a nonlinear dimensional reduction technique.

Genotyping

Genomic DNA was extracted from fibroblasts using QIAamp DNA Mini Kit (Qiagen). PCR was performed using Phusion DNA polymerase (NEB) following the published protocol, with amplification primers (see Table S3) at the annealing temperature of 63°C for 35 cycles. PCR product was run on 1% agarose gel to confirm size and product was extracted using QIAquick Gel Extraction Kit (Qiagen). For restriction digest test, 500ng of PCR product was then digested with NspI (NEB) then run on a 1% gel and imaged. For sequencing, purified PCR product was submitted to GeneWiz with sequencing primer (see Table S3) and resulting tracks were visualized compared to control *MAPT* sequence.

RNAseq cell collection, sequencing, data processing, and analysis

MiNs were collected on PID21 in triplicate for RNA-sequencing using RNeasy Plus Micro Kit (Qiagen) according to the manufacturer's instructions. Cortical glutamatergic iPSC-Ns were purchased from BrainXell (BX-0300e), human adult whole brain RNA was purchased from Biochain (R1234035-50), and human fetal brain RNA sample was purchased from Cell Applications (1F01-50). Adult human brain and fetal brain RNA samples were run by GTAC through the NovaSeq6000 using SMARTer 150PE with 30 million reads per sample input. MiNs and iPSC-Ns were sequenced by DNALink (www.dnalink.com) on NovaSeq6000 using SMARTer 100PE and 40-50 million reads per sample input.

FastQC (http://www.bioinformatics.babraham.ac.uk/projects/fastqc) was used to determine sequencing quality and identify adapter contamination and FastQ files were trimmed using cutadapt for adapter contamination (if needed). Trimmed sequences were mapped to hg38 using STAR (Dobin and Gingeras, 2015). Raw gene counts were extracted using deepTools multiBamSummary option –outRawCounts ((Ramírez et al., 2016). Differential gene expression analysis was performed using DESeq2 normalizing to sequencing depth (Love et al., 2014). Genes defined as differentially expressed had an adjusted p-value < 0.05. Genes were categorized as RNA binding or splicing regulators by Ingenuity Pathway Analysis (QIAGEN).

Leafcutter data processing and analysis

New BAM files were generated by STAR using the –outSAMstrandField intronMotif option were used for Leafcutter (Li et al., 2018), according to the published and recommended protocol (https://davidaknowles.github.io/leafcutter/). Samples were grouped by both cell-type and age and comparisons were performed pairwise, as required for Leafcutter analysis. Differentially spliced clusters and introns were defined by FDR < 0.05, were exported using LeafViz by Jack Humphry (https://github.com/jackhump/leafviz), and loci colors were edited using illustrator (Adobe). Splicing line weights were linearly-scaled so all clusters had similar line weights for easier viewing. Per cluster, cryptic splicing events with less than 5% inclusion were removed.

Semi-quantitative PCR (sq-PCR)

Semi-quantitative PCR was performed to quantify the ratio of 3R:4R mRNA. To perform sqPCR, cDNA was generated from RNA (SuperScript IV Reverse Transcriptase, Thermo Fisher 18090010) then amplified using primers (Choi et al., 2014) flanking exon 10 (forward 5′-AAGTCGCCGTCTTCCGCCAAG-3′; reverse 5′-GTCCAGGGACCCAATCTTCGA-3′). The PCR product was then run on a 2% agarose gel with 381bp and 288bp fragments indicating 4R and 3R, respectively. Ratios were then calculated as previously described (Antiabong et al., 2016), via imageJ box plots and measure plots, summed pixel intensity values were exported to Excel, where each isoform value was divided by the summed total to generate percentage of each isoform. N isoform primers for sqPCR: forward 5′-TACGGGTTGGGGGACAGGAAACAT-3′; reverse 5′- GGGGTGTCTCCAATGCCTGCTTCT-3′.

Lysate Preparation for mass spectrometry analysis

MiNs were collected on PID 30. iPSC-Ns were collected after six weeks. Both were collected in the same manner. Briefly, media was removed and cells were washed once with DPBS. Fresh DPBS was added to the wells and cells were scraped off. Resuspended cells were pelleted at 1000g for 5min at RT, supernatant was removed, and pellets were frozen at -80°C until use.

Three different lots of Human Primary Neurons were purchased from ScienCell and plated according to manufacturer's instructions. Cells were cultured in Neuronal Medium (ScienCell #1521) for one week and collected same as the miNs and iPSC-Ns.

Adult brain frozen tissues was sliced via a cryostat at -20°C, from which 300-400mg was sonicated in 4°C buffer containing 25mM tris-hydrochloride (pH 7.4), 150 mM sodium chloride, 10 mM ethylenediaminetetraacetic acid, 10 mM ethylene glycol tetraacedic acid, phosphatase inhibitor cocktail, and protease inhibitor cocktail, with final brain suspension at 0.3 mg/μL buffer. Suspension was cleared using centrifugation for 20 minutes at 11,000 g at 4°C and the resulting supernatant was defined as "brain homogenate" (Horie et al., 2020).

Immunoprecipitation and mass spectrometry of tau isoforms

Mass spectrometry analyses of tau proteins were performed as previously described with some modifications (Barthélemy et al., 2020a, 2020b; Horie et al., 2020; Sato et al., 2018). Cells and brain homogenates were diluted with PBS and 2% human serum albumin (Sigma D4197) respectively, and lysed with final concentration of 0.5% NP-40 and 2.5mM guanidine. Tau protein was immunoprecipitated with mouse anti-Tau (Tau1) (provided by Dr. Nicholas Kanaan, 1.125μg/sample), and mouse anti-human tau (HJ8.5) (provided by Dr. David Holtzman, 2.25μg/sample), digested with trypsin, oxidized, desalted and subjected to nano-Acquity LC and MS analyses using Orbitrap Eclipse Tribrid Mass Spectrometer (Thermo Scientific). Mass spectrometry data were extracted using Skyline software (Maclean et al., 2010).

All samples were spiked with full length ^{15}N-labeled 2N4R recombinant tau as an internal standard and ratios of isoforms were calculated by using 2N and 4R isoform-specific peptides compared to constitutive peptides (all peptide numbers are in reference to 2N4R isoform). For 2N, the 2N-specific tryptic peptide 68-87 was divided by the common peptide 151-155 to obtain percentage of 2N. 1N isoform percentage was calculated by dividing a shared 1N/2N peptide, 45-67, by the common peptide 151-155, to obtain the cumulative percentage of 1N+2N isoforms. The previously calculated 2N percentage was subtracted from this shared 1N/2N percentage to calculate the 1N percentage. 0N percentage was calculated by subtracting both 1N and 2N percentages from 100. Percent 4R was calculated three ways by dividing each of the R2 region, 4R-specific peptides, 275-280, 282-290, and 299-317, by the constitutive adjacent R1 peptide, 260-267. 3R was calculated by subtracting the 4R percentage from 100.

Immunoblot analysis

Media was aspirated from wells, cells were washed with DPBS, and lysed in the plate with RIPA (Sigma #R0278) supplemented with cOmplete Mini Protease Inhibitor Cocktail (Roche #11836153001). Lysate was collected and centrifuged at 13,000g for 10 minutes at 4°C. BCA protein assay determined protein content and samples were normalized with RIPA/protease inhibitor. Samples were treated with Lambda Phosphatase (NEB #P0753L) for 3 hours at 30°C. LDS NuPAGE sample buffer with 5% β-mercaptoethanol was added and samples were heated to 95°C for 3 minutes then loaded onto a NuPAGE 8% 20-well Midi gel (Invitrogen WG1002), with Tau Peptide Ladder (rPeptide T-1007-2). After running, the gel was transferred onto either 0.45um PVDF membrane for 2hr at 400mA. Membrane was both blocked and treated with primary antibodies in TBS/0.1% Tween20 overnight at 4°C: rabbit anti-Tau antibody (Aligent/DAKO, A002401-2 1:1000-10,000). The next day, membrane was washed 3 times with TBST, then treated with peroxidase-conjugated goat anti-rabbit secondary antibodies in 5% Milk/TBS/0.1% Tween 20 for up to 3hrs at RT. Membrane was washed 3 times with TBS/0.1% Tween20 and developed with the ECL system (Thermo Scientific, #34076) and imaged on a Sapphire Imager (Azure Biosystems).

Biosensor cell culture methods

MiNs were harvested on PID 26 in 50 mM Tris-HCl, pH 7.5 150 mM NaCl. The lysates were sonicated for 4.5 minutes at 50% amplitude (QSonica, Q800R3 Sonicator). BCA assay was used determine protein concentration of protein. HEK biosensor Tau RD-CFP/YFP cell line, kindly provided by Dr. Marc Diamond (Furman et al., 2015), were cultured in 10 cm dish in DMEM (+Pyruvate, + D-glucose/D-glutamine) (Thermofisher) with 10%FBS and 1% Pen-Strep. The day before the seeding experiment, cells were replated in a 96-well plate at a density of 40,000 cells/well in 130uL of media and left adhere over-night. The following day, cells were seeded with miN lysates; the seeding mixes were made by combining 17μg of total protein lysate per well to 3.75μL of Opti-MEM (Gibco) and 1.25uL Lipofectamine 2000 (Invitrogen) for a total volume of 20 μL per well. Liposome preparations were incubated at room temperature for 30 min before adding to cells, and each condition was done in triplicate. Cells were incubated with seeding mixes for 72 h before the analysis.

FRET flow cytometry

After 72 h from the seeding, cells were washed in PBS (Gibco), harvested with 0.25% trypsin and fixed in 4% paraformaldehyde for 10 min, then resuspended in flow cytometry buffer (1 mM EDTA in PBS). The BD LSRFortessa™ Flow Cytometer was used to perform FRET flow cytometry as previously described (Furman et al., 2015). Briefly, to measure CFP and FRET, cells were excited with the 405 nm laser, and to measure YFP cells were excited with a 488 laser. Fluorescence was captured with a 405/50 nm, 525/50 nm and 525/50 nm filters respectively.

To quantify FRET, a gating strategy similar to that previously described was used (Furman et al., 2015): first the CFP bleed-through into the YFP and FRET channels was compensated, and cells were gated in order to exclude YFP-positive only cells emitting in the FRET signal. A bivariate plot of FRET vs. CFP was made to assess the number of FRET-positive cells. The percentage of FRET (i.e., the number of FRET-positive cells per total cell count) and the Integrated FRET density (i.e. product of percent positivity and median fluorescence intensity) were used for the analyses. Data analysis was performed using FCS Express 7 Research software (De Novo Software).

Immunocytochemistry, imaging and analysis

Methanol fixed cells in DPBS had the liquid tipped off, and the cells were blocked with 200 μL/well of Intercept Blocking Buffer (LI-COR) containing 0.1% Triton for one hour at room temperature. The primary antibodies (see STAR Methods) were prepared in Blocking Buffer and incubated overnight at 4°C with gentle agitation.

On the following day, the primary antibody was tipped off, and the cells were washed three times with 200 μL/well of DPBS. The secondary antibodies Goat anti-mouse IgG2b 647 Alexa Flour-conjugated antibody (A-21242) and Goat anti-rabbit 488 Alexa Flour-conjugated antibody (A-11008), as well as Hoechst 33342 (Invitrogen) were prepared at 1:1000 in Blocking Buffer and left for 1 hour at room temperature.

The plates were then washed three times with 200 μL/well of DPBS, before being left in DPBS at 4°C until high-content imaging using the Opera Phenix (Perkin Elmer). Images were taken using a 20X water objective, with 75 fields of view per well, and a Z-stack of 6 slices. The images were analysed using Perkin Elmer software Harmony as previously described (Katsikoudi et al., 2020). Briefly, stacks of each image were maximum projected and filtered using the sliding parabola to smoothen the background and get rid of the fluorescent noise. Subsequently, machine learning was used to define the tau positive area used as region in which the software was trained to identify the tau positive threads (for TOC1, only cytoplasmic signal was included in the analysis). Total nuclei were also detected and analyzed. At the end of the analysis results were exported in an Excel file divided by object (total nuclei and tau count) and well. The final readout was ''Tau count normalized to the total nuclei count''. Any well with fewer than 800 nuclei was not included in analysis. n=total number of nuclei per line. Data was plotted in GraphPad.

STED microscopy

STED microscopy was performed on a Leica STELLARIS 8 STED. Cells were methanol fixed as previously described. Primary antibodies were used at 1:1000. Secondary antibody was purchased from Abberior and used at 1:250.

SiRNA treatment of miNs

MiNs were replated, as per the above protocol, at PID 5 on 24 well Sensoplate (Greiner, 662892) previously coated with poly-ornithine, laminin, and fibronectin.

At PID 18, cells were treated with 1uM of Dharmacon™ Accell™siRNAs: Accell Human MAPT (4137) siRNA-SMARTpool (E-012488-00-0050) and Accell Non-targeting Pool (D-001910-10-05). Treatment was left on until PID 26 when cells were fixed with 100% methanol to extract soluble proteins, as described previously (Guo et al., 2016; Katsikoudi et al., 2020). In brief, the growth media was completely aspirated, and cells were washed twice with 200 μL/well of DPBS. Ice-cold 100% methanol was added 200 μL/well for 15 minutes at room temperature. Subsequently, the cells were washed three times with 200 μL/well of DPBS, with the final wash being left on for storage. Plates were kept at 4C° until immunocytochemistry (ICC) was performed.

QUANTIFICATION AND STATISTICAL ANALYSIS

Two-tailed Student's t-test were performed for datasets containing two groups. ANOVA analyses were used for datasets with more than two groups. Specific statistical details and n information for each assay can be found in the corresponding figure legends and methods sections. All data is presented as mean±SEM. Differences were considered statistically significant at *$p<0.05$, **$p<0.01$, ***$p<0.001$.

Cell Stem Cell, Volume *29*

Supplemental Information

Recapitulation of endogenous 4R tau expression and formation of insoluble tau in directly reprogrammed human neurons

Lucia S. Capano, Chihiro Sato, Elena Ficulle, Anan Yu, Kanta Horie, Ji-Sun Kwon, Kyle F. Burbach, Nicolas R. Barthélemy, Susan G. Fox, Celeste M. Karch, Randall J. Bateman, Henry Houlden, Richard I. Morimoto, David M. Holtzman, Karen E. Duff, and Andrew S. Yoo

Figure S1. Related to Figure 1

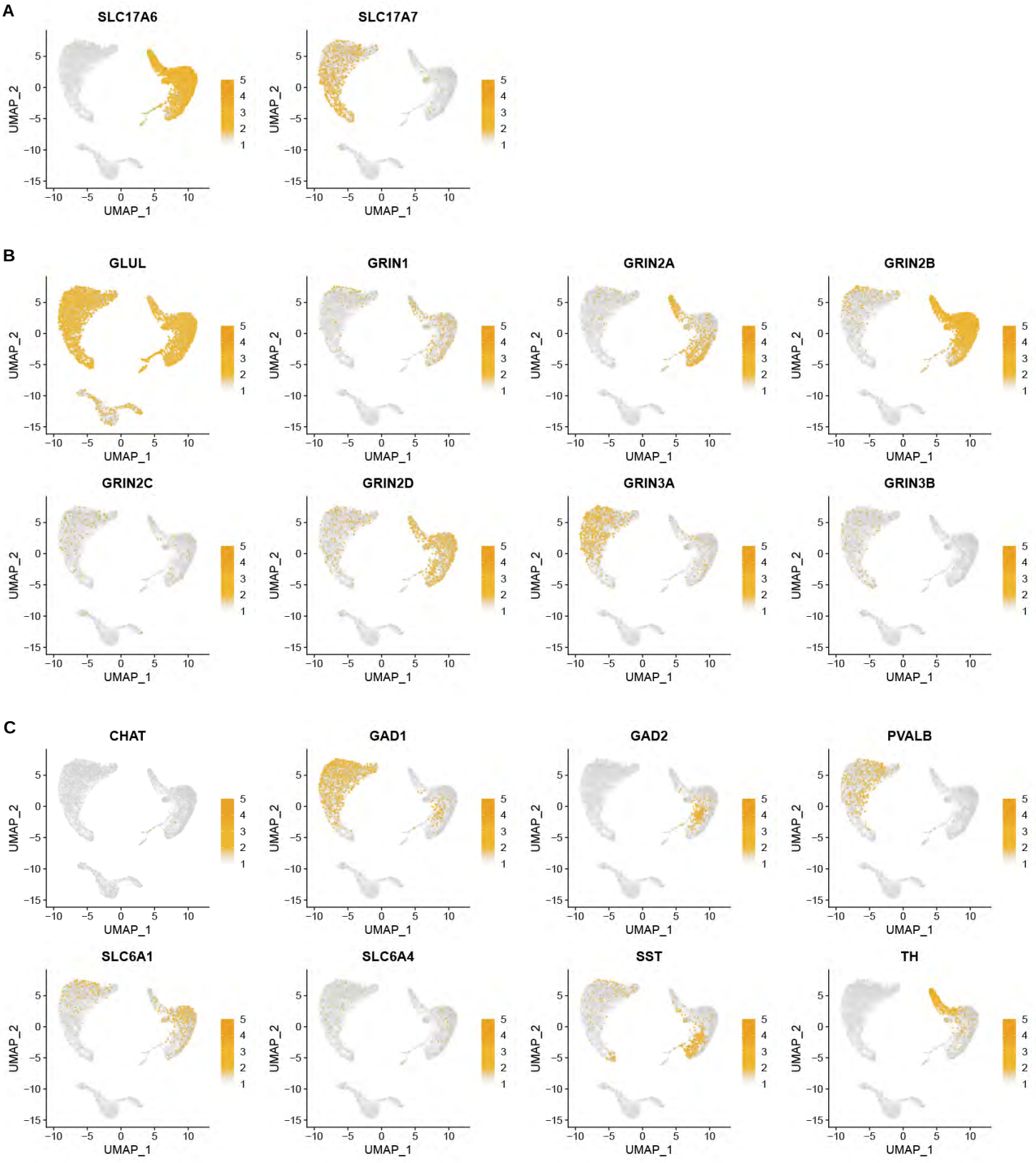

Figure S1. Single cell RNAseq subtyping, Related to Figure 1

(A) UMAP of the glutamatergic markers SLC17A6 (VGLUT2) and SLC17A7 (VGLUT1) across cell populations.

(B) Additional glutamatergic marker expression including GLUL, and the NMDA receptor subunits GRIN1, GRIN2A, GRIN2B, GRIN2C, GRIN2D, GRIN3A, GRIN3B.

(C) Expression patterns of non-glutamatergic neuronal lineages, including the cholinergic marker CHAT, inhibitory markers GAD1, GAD2, PVALB, SLC6A1, SST, serotonergic marker SLC6A4, and dopaminergic marker TH.

See also Figure 1.

Figure S2. Related to Figure 2

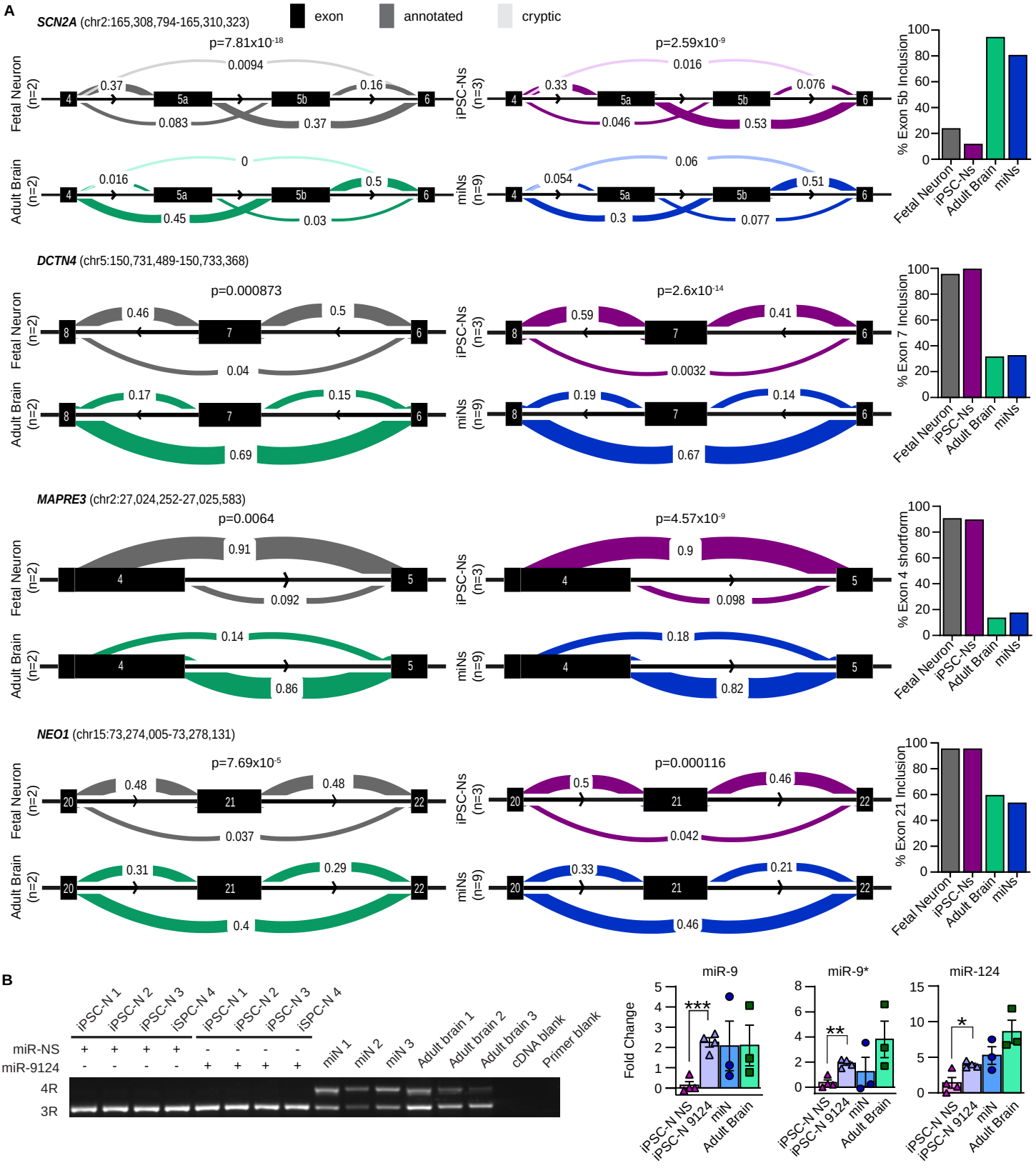

Figure S2. Age-associated splicing events in miNs and 4R expression independent of miRNA over-expression, Related to Figure 2

(A) Differential splicing events between fetal neurons and iPSC-Ns compared to adult brain and miNs. Examples include SCN2A, DCTN4, MAPRE3, and NEO1.

(B) Left, semi-quantitative PCR of 3R and 4R tau isoforms in differentiated iPSC-Ns with overexpression of either nonspecific miRNAs (miR-ns) or miRNAs-9/9*-124 (miR-9124) demonstrating no expression of 4R tau in either condition. Right, qPCR validating the overexpression of miRs-9, -9*, and -124.

See also Figure 2 and Tables S1 and S2

Figure S3. Related to Figure 4

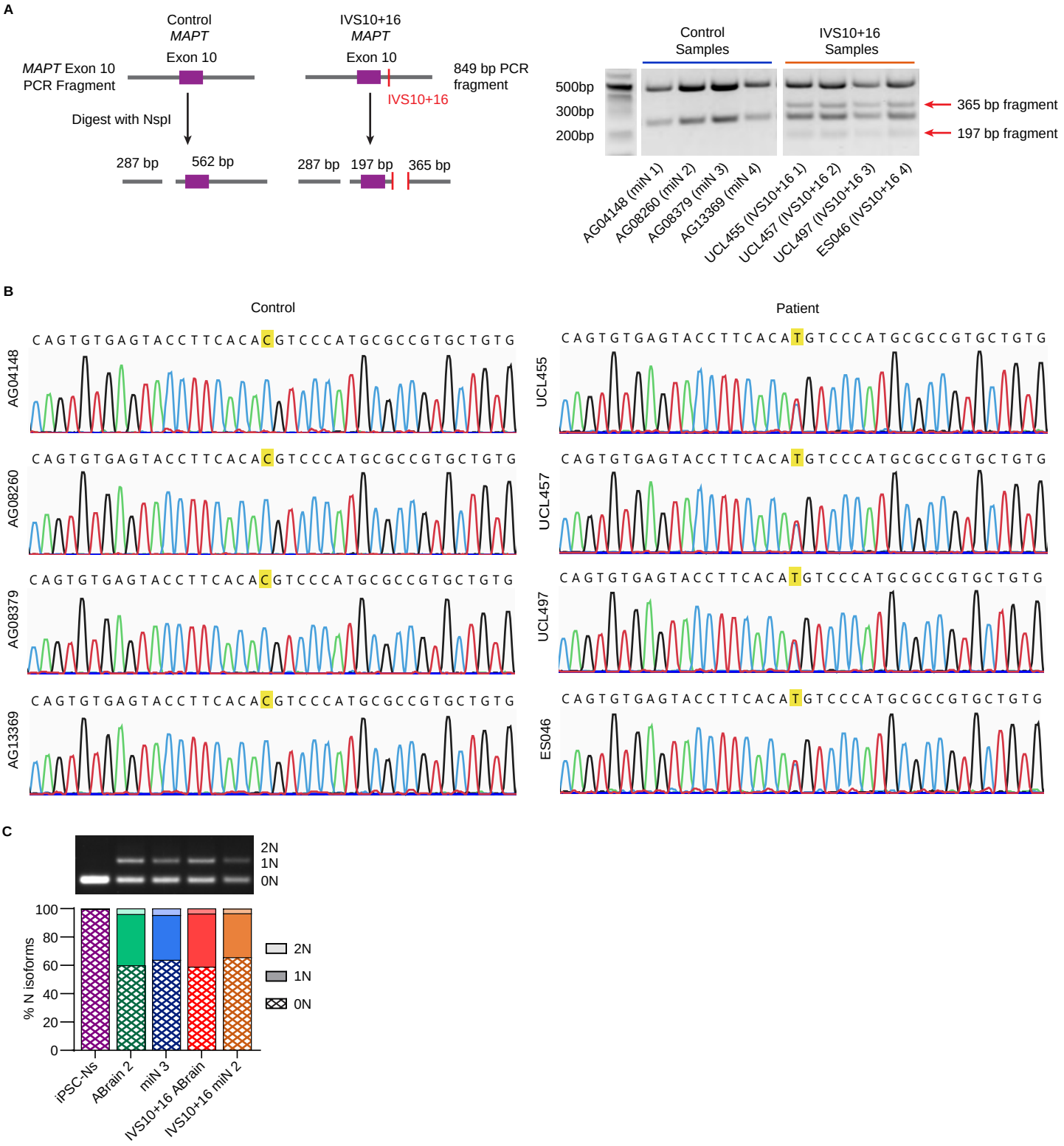

Figure S3. Confirmation of mutational status in control and IVS10+16 fibroblasts and comparison of N isoform expression, Related to Figure 4

(A) Diagram explaining restriction digest genotyping for IVS10+16 C>T mutation, which creates a novel NspI site, as previously published (Hutton et al., 1998). PCR fragment is generated from genomic DNA and digested with NspI. Control samples produced two bands, whereas patient samples had four, corresponding to heterozygous status.

(B) Sanger sequencing of IVS10+16 and surrounding region in MAPT for all lines confirms the presence of IVS10+16 C>T mutation in patient samples, where two peaks were present at the 10+16 location representing C and T. This mutation and no other MAPT mutations were present with exon 10 or in the known intronic mutation sites.

(C) Semi-quantitative PCR of N isoforms between fetal, healthy, and IVS10+16 samples. No significant change was detected.

See also Figure 4.

Figure S4. Related to Figure 6

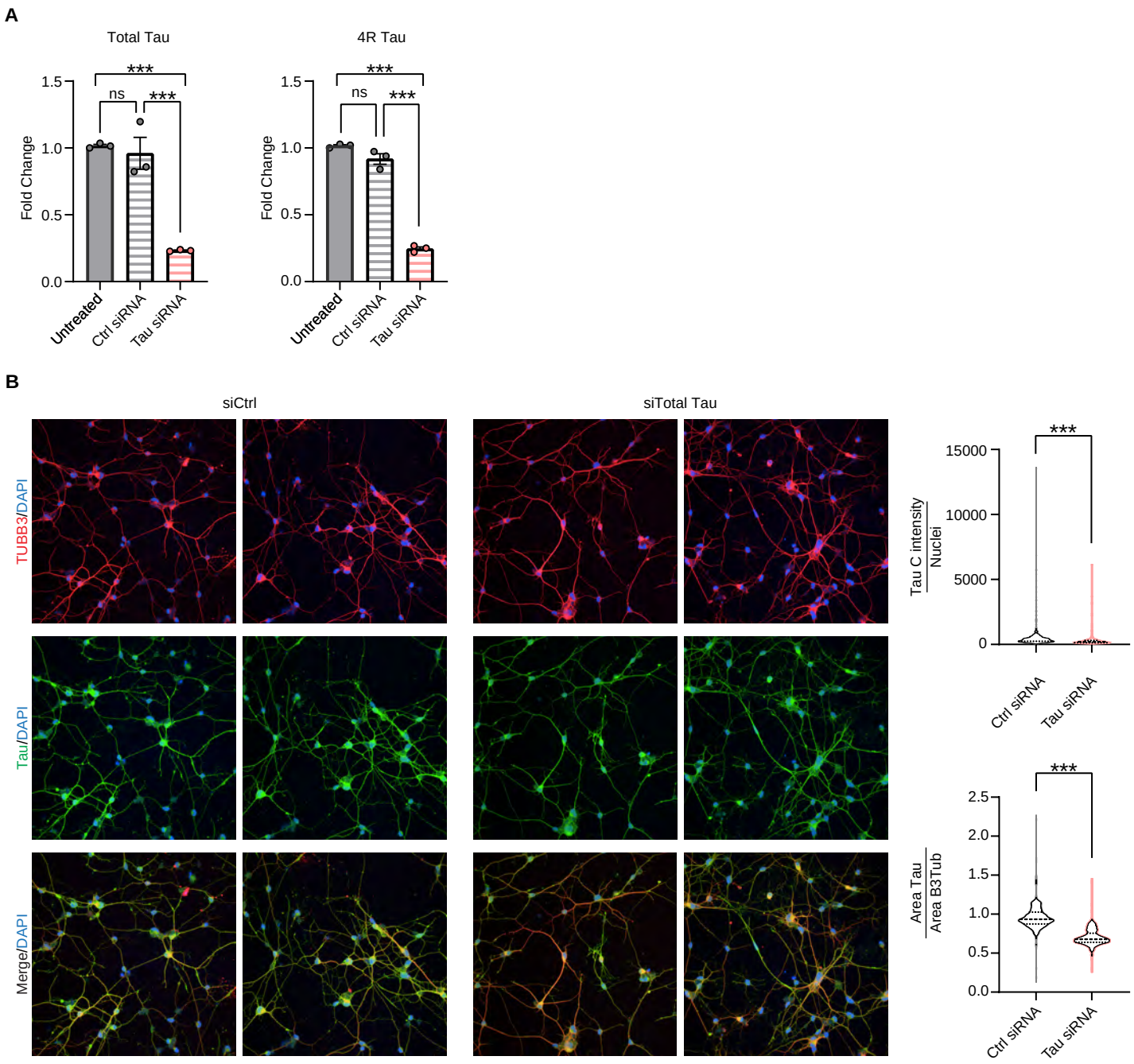

Figure S4. siRNA against total tau shows reduction in both mRNA and protein levels, Related to Figure 6

(A) qPCR of control miNs either untreated (solid grey), treated with siControl (grey stripe), or siTotal tau (pink stripe) for their total tau and 4R tau expression relative to untreated. ***p < 0.001.

(B) Immunocytochemistry of PFA-fixed control miNs treated with siControl (grey) or siTotal tau (pink) show a reduction in total tau fluorescent intensity compared to both total nuclie and total TUBB3 area. N=380-395 images per condition. Nuclei count: siControl=9982; siTotal tau=12362. ***p < 0.001.

See also Figure 6.